PREPARED FOR THE U.S. DEPARTMENT OF ENERGY,
UNDER CONTRACT DE-AC02-76-CHO-3073

PPPL-2805
UC-427

PPPL-2805

THE EFFECTS OF PLASMA DEFORMABILITY ON THE FEEDBACK STABILIZATION OF AXISYMMETRIC MODES IN TOKAMAK PLASMAS

BY

D.J. WARD AND S.C. JARDIN

January 1992

PPPL PRINCETON PLASMA PHYSICS LABORATORY

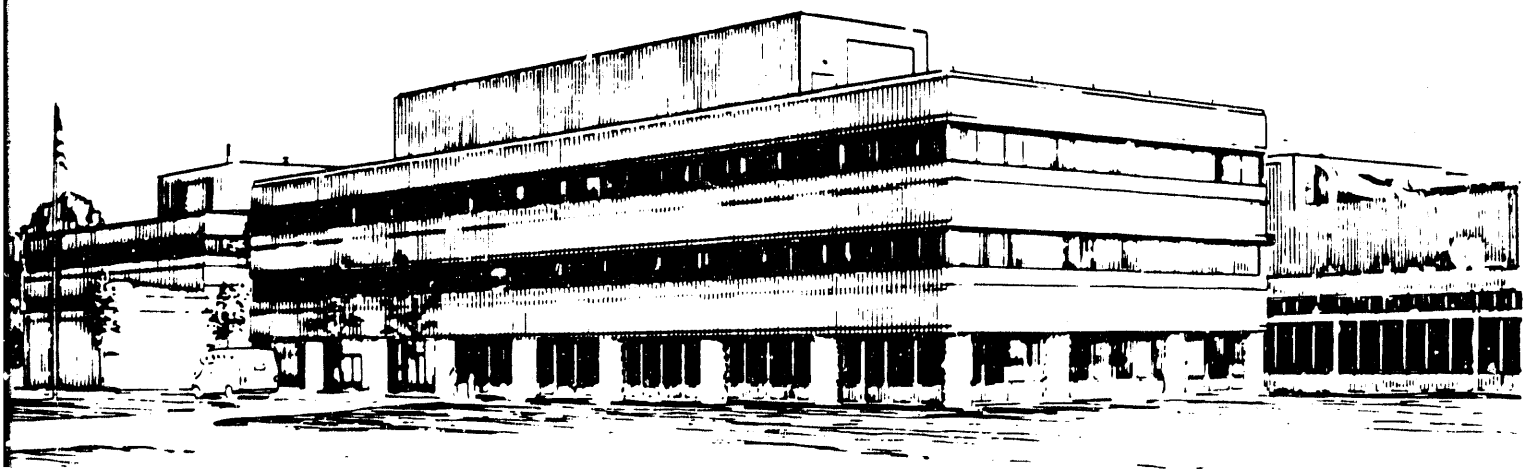

NOTICE

NOTICE

The Effects of Plasma Deformability on the Feedback Stabilization of Axisymmetric Modes in Tokamak Plasmas

PPPL--2805

DE92 006812

D. J. Ward

Centre de Recherches en Physique des Plasmas,

Association Euratom–Confédération Suisse,

Ecole Polytechnique Fédérale de Lausanne,

21 av. des Bains, 1007 Lausanne, Switzerland

S. C. Jardin

Plasma Physics Laboratory, Princeton University

P.O. Box 451, Princeton, New Jersey 08543, USA

Abstract

The effects of plasma deformability on the feedback stabilization of axisymmetric modes of tokamak plasmas are studied. It is seen that plasmas with strongly shaped cross sections have unstable motion different from a rigid shift. Furthermore, the placement of passive conductors is shown to modify the non-rigid components of the eigenfunction in a way that reduces the stabilizing eddy currents in these conductors. Passive feedback results using several equilibria of varying shape are presented. The eigenfunction is also modified under the effects of active feedback. This deformation is seen to depend strongly on the position of the flux loops which are used to determine plasma vertical position for the active feedback system. The variations of these non-rigid components of the eigenfunction always serve to reduce the stabilizing effect of the active feedback system by reducing the measurable poloidal flux at the flux-loop locations. Active feedback results are presented for the PBX-M tokamak configuration.

1. Introduction

It is well known that shaping the tokamak cross section allows increasing the total plasma current, which implies both increased maximum stable β values and increased energy confinement time. This has been demonstrated both theoretically and experimentally [1–5]. However, tokamak plasmas with any significant cross-sectional shaping are subject to troublesome axisymmetric instabilities which must be stabilized by a conducting wall near the plasma and by an active feedback system to compensate for the resistive losses in these conductors [6].

The axisymmetric instability has been studied in great detail with regard to stabilization with passive conductors [7–15] and an active feedback system [14–20]. However, most studies have been limited in one way or another. Linear MHD stability codes [21,22], which can accurately treat the plasma motion, have mostly been limited to ideal

configurations in which there is an ideally conducting wall and no active feedback system (or one which is limited to special, unrealistic symmetry constraints [16,23]). Most other models which include realistic circuit equations for the passive conductors treat the plasma in some simplified fashion which does not account for the true plasma motion. This usually involves modeling the plasma as a collection of current filaments and/or prescribing some simplified (usually rigid) plasma motion. Even the sophisticated active feedback system [19,20] used for the optimization of plasma shape and β in DIII-D [5] is based upon an assumed rigid motion of the plasma. Transport time-scale simulation codes such as the Tokamak Simulation Code (TSC) [18] can accurately compute the full nonlinear axisymmetric motion with all the realistic control aspects such as an active feedback system, resistive conductors, circuit and power supply dynamics. However, it is computationally expensive and difficult to obtain linear growth rates and very difficult to resolve the details of the plasma motion with these comprehensive nonlinear codes.

It is known that the true unstable motion of highly shaped tokamak plasmas involves non-rigid deformations [24]. The non-rigid components of the motion can be affected, and even enhanced, by certain aspects of a feedback system. It has been shown [23] that for certain locations of the detectors which control the active feedback system, even though able to detect a rigid plasma motion, the detectors are ineffective in detecting the motion of a deformable plasma, and the feedback system is unable to stabilize the plasma regardless of the feedback gain. This was found to be due to a deformation in the motion dictated by the details of the active feedback system itself. Experimentally it has been reported that the further optimization of plasma shape in DIII-D may be limited by the difficulties in detecting and controlling a significant nonrigid component to the plasma motion [20].

In this paper we study the linear MHD stability of the axisymmetric mode in tokamak plasmas with realistic passive conductors and active feedback systems. We focus on the effects of passive conductors and active feedback on the eigenfunction of the instability. It is shown that the eigenfunction is modified in each case in such a way that the stabilizing

effects of the particular feedback system are reduced.

To perform this study we use the NOVA-W stability code [25]. This linear MHD stability code includes the effects due to realistic resistive conductors and an active feedback system in the vacuum region. The following section gives a brief overview of the NOVA-W calculation, outlining the calculation of the vacuum boundary condition. However, the reader is referred to Ref. [25] for a complete description of the formulation, numerical calculation, convergence studies, and the code comparisons to analytic and numerical models demonstrating its accuracy and utility.

Section 3 focuses on a study of the effect of the position of discrete passive conductors on the instability eigenfunction and growth rate. We examine three equilibria of differing shape and aspect ratio. For a particular position of a pair of discrete passive conductors, we show that the plasma eigenfunction is modified to reduce the stabilizing effects of the conductors.

It is important to understand and to be able to predict the most effective location for placement of discrete conductors for passive stabilization. In a reactor design, for example, the space near the plasma is valuable, and it would be desirable to reduce the volume of passive conductors that must lie close to the plasma. It is therefore of interest to understand how different passive conductor configurations affect the eigenfunction and the growth rate. This analysis is not only important for the case of individual discrete conducting plates, but also for the case of a complete conducting shell. The analysis provides insight on where one might increase the wall thickness to significantly improve the passive stabilization without everywhere increasing the thickness which might have otherwise detrimental effects.

In Section 4 we study the effects of an active feedback system on the PBX-M equilibrium. Varying the position of the flux-loop detectors which measure the plasma vertical position is shown to change the deformation that the eigenfunction experiences due to the feedback system. These deformations are such that the measurable signal at the

flux loops, and thus the ability of the feedback system to detect vertical displacement, is reduced. This confirms the conclusion of Ref. [23] for a similar PBX-M equilibrium, but here we explicitly show the eigenfunction deformation and how it affects the effectiveness of the feedback system.

2. Numerical Formulation

The NOVA-W stability code solves the linear ideal MHD stability eigenvalue equations

$$\rho\omega^2\vec{\xi} = \nabla p_1 + \vec{b}\times(\nabla\times\vec{B}) + \vec{B}\times(\nabla\times\vec{b}) \tag{1}$$

$$p_1 + \vec{\xi}\cdot\nabla P + \gamma P\nabla\cdot\vec{\xi} = 0, \tag{2}$$

where

$$\vec{b} = \nabla\times(\vec{\xi}\times\vec{B}) \tag{3}$$

is the perturbed magnetic field in the plasma, $\vec{B}$ is the equilibrium magnetic field, p_1 and P are the perturbed and equilibrium particle pressures, respectively, ρ is the plasma mass density, $\gamma = \frac{5}{3}$ is the ratio of specific heats, $\vec{\xi}$ is the displacement vector, and ω is the eigenvalue (normalized growth rate). The equilibrium magnetic field is represented by

$$\vec{B} = \nabla\zeta\times\nabla\psi + q(\psi)\nabla\psi\times\nabla\Theta \tag{4}$$

or

$$\vec{B} = \nabla\phi\times\nabla\psi + \mathrm{g}(\psi)\nabla\phi, \tag{5}$$

where $2\pi\psi$ is the poloidal flux contained within a surface, Θ is the generalized poloidal angle, ζ is the generalized toroidal angle, ϕ is the standard toroidal angle from (X,ϕ,Z) cylindrical coordinates, $q(\psi)$ is the safety factor, and $\mathrm{g}(\psi)$ is the toroidal field function. The second definition for $\vec{B}$, Eq. (5), follows for an axisymmetric equilibrium. The generalized angle coordinates (Θ,ζ) are chosen to make the magnetic field lines appear straight in this coordinate system.

We use an axisymmetric flux formulation for the perturbed vacuum magnetic field. This is the natural representation for the axisymmetric mode and allows the existence of perturbed axisymmetric (feedback) currents in the vacuum. The perturbed flux also allows simple boundary conditions for a thin wall approximation of the resistive wall, and allows the use of flux difference measurements as the measurement of perturbed position. Therefore the perturbed magnetic field in the vacuum is represented by

$$\vec{b} = \frac{1}{2\pi}\nabla\phi \times \nabla\chi + \mathrm{a_t}\nabla\phi, \tag{6}$$

where χ is the perturbed poloidal flux in the vacuum and $\mathrm{a_t}$ is the perturbed toroidal component.

One can relate the perturbed flux χ to the sum of all the perturbed currents in the vacuum region and Green's integrals over the boundary surfaces of the vacuum region:

$$\chi(\vec{r}) = \sum_{i=1}^{N} \mu_0 I_i G(\vec{r};\vec{r}_i) + \sum_S \frac{1}{2\pi}\oint_S \frac{dl_S}{X_S}[\chi\nabla_n G(\vec{r};\vec{r}_S) - G(\vec{r};\vec{r}_S)\nabla_n\chi]. \tag{7}$$

Here, $G(\vec{r};\vec{r}_S)$ is the toroidal Green's function for this problem. The three boundary surfaces consist of the plasma-vacuum interface, the inside surface of the resistive wall, and the outside surface of the resistive wall. Here $\nabla_n = \hat{n}\cdot\nabla$ where $\hat{n}$ is the unit vector normal to the surface, and the feedback currents are defined as linear combinations of the perturbed flux and the corresponding time-derivative terms at prescribed observation points. Perturbed magnetic field measurements (magnetic probe measurements) can also be included in the feedback law. As an example we can consider a simple feedback law in which the desired current for a given feedback coil is proportional to the difference in the perturbed flux (and its time derivative) at two observation points symmetric about the midplane. This flux difference serves as a measure of the vertical displacement of the plasma, and can be very accurate in the case of rigid plasma motion. In this case the feedback currents are defined as

$$I_m = \alpha_m[\chi(X_{o1},Z_{o1}) - \chi(X_{o2},Z_{o2})] + \beta_m[\dot{\chi}(X_{o1},Z_{o1}) - \dot{\chi}(X_{o2},Z_{o2})]. \tag{8}$$

The boundary condition at the resistive wall is found by using the thin-wall approximation. This leads to an expression relating the jump in the normal derivative of the flux at the resistive wall to the perturbed flux at the wall:

$$[[(\hat{n}\cdot\nabla\chi)]] = 2\pi X^2\mu_0\delta_w\vec{J}\cdot\nabla\phi = \frac{\mu_0\delta_w}{\eta}\frac{\partial\chi}{\partial t} = -i\omega\mu_0\frac{\delta_w}{\eta}\chi_w, \tag{9}$$

where $[[\cdots]]$ denotes the jump across the thin resistive wall, δ_w is the thickness, and η is the resistivity of the wall.

The boundary condition required by NOVA to solve the eigenvalue equations is to relate the Fourier components P_{1m} of the total perturbed pressure to the components $\xi_{\psi m}$ of the radial displacement ξ_ψ at the plasma-vacuum interface. The perturbed pressure P_1 at the P-V interface is found in terms of the normal derivative of the flux at the boundary:

$$P_1 = \vec{B}\cdot\vec{b} = (\nabla\phi\times\nabla\psi)\cdot(\nabla\phi\times\frac{\nabla\chi}{2\pi}) + g(\psi_{edge})\nabla\phi\cdot a_t\nabla\phi, \tag{10}$$

$$= \frac{|\nabla\psi|}{2\pi X^2}\nabla_n\chi + a_t g(\psi_{edge})\frac{1}{X^2}$$

where ψ_{edge} is the value of ψ at the plasma-vacuum boundary. Similarly, the normal component of the displacement of the plasma boundary is related to the perturbed poloidal flux at the boundary by

$$\xi_\psi = \vec{\xi}\cdot\nabla\psi = \sum_m \xi_{\psi m}\exp(im\Theta) = -\frac{1}{2\pi}\chi. \tag{11}$$

The goal of the vacuum calculation is to find $\nabla_n\chi$ in terms of χ at the plasma-vacuum boundary. This then gives the required relationship between P_1 and ξ_ψ through Eqs. (10) and (11). The reader is referred to Ref. [25] for details on this calculation including specifics on the passive conductors and the feedback system in the calculation.

3. Non-rigid effects on passive stabilization

In this section we will examine how variations in the passive conductor configuration alters the form of the eigenfunction and how this affects overall stability. We consider

first a very large aspect ratio ($A = 100$) elliptical equilibrium with elongation $\kappa = 2.0$ and with a nearly flat current profile. This equilibrium was used [25] for comparison of NOVA-W calculations to a simplified analytic model [12]. With this equilibrium we can consider the effects of the deformability of the eigenfunction with respect to variations in the passive conductors without the effects of toroidicity or triangularity. Next we will consider toroidal effects with an elliptical equilibrium at lower aspect-ratio, and finally the CIT design equilibrium which has significant triangularity in addition to toroidicity. The wall contour for both of the elliptical equilibria is a concentric ellipse with the distance between the wall and the plasma on the midplane equal to one half the plasma minor radius. The wall contour for the CIT equilibrium corresponds to the design vacuum vessel contour, as was used in previous studies [25,26], but with a uniform thickness.

The NOVA-W code calculates the linear eigenfunction of the instability as a sum over poloidal harmonics: $\xi_\psi = \sum_m \xi_{\psi m} \exp(im\Theta)$. For configurations completely symmetric about the midplane (the only configurations considered here) this sum can be reduced to a sum over $\sin(m\Theta)$. For an infinite-aspect-ratio plasma with a circular cross-section, a rigid shift would be represented by a pure $m = 1$ component in the eigenfunction. However, for the more complicated cross-sectional shapes at finite aspect ratio that we consider here, a rigid shift, when decomposed into Fourier poloidal harmonics of the equal-arc-length magnetic coordinate system, is not a pure $m = 1$ mode. This rigid shift is still dominated by the $m = 1$ component, but there are higher m contributions as well.

3.1. A very large aspect-ratio ellipse

We demonstrate here that when only a small conducting segment of the wall is present, there is a strong dependence of the normalized magnitude of the $m > 1$ components on the poloidal position of the plate. There is also a drastic variation in the growth rate with respect to the poloidal position. In order to study this phenomenon in detail, we performed a series of calculations in which there is only a single pair of up-down symmetric

conducting sections of the wall. The length of each of these conducting "plates" is approximately 1/8 of the circumference of the complete wall contour, and has a resistance equal to a 1 cm thickness of aluminum. The ratio δ/η is reduced over a few grid points from the value of the conducting plate to the value of the "vacuum." This helps to avoid numerical difficulties. In each calculation the plates are centered at a different poloidal location $|\Theta|$, where Θ is measured with respect to the outboard midplane. The value of $|\Theta|$ is changed, between calculations, in increments from $|\Theta| = 0$ at the outboard midplane to $|\Theta| = \pi$ at the inboard midplane. We are particularly interested in how the non-rigid components of the motion change with regard to the variation of the passive conductor position. To characterize these variations we show the changes in the ratios of the $m \neq 1$ components to the $m = 1$ component of the eigenfunction, $\xi_{\psi m}/\xi_{\psi 1}$, measured at the plasma edge.

The very large aspect-ratio ellipse results are shown in Fig. 1. The figure shows the computed values of $\xi_{\psi 2}/\xi_{\psi 1}$ and $\xi_{\psi 3}/\xi_{\psi 1}$ as a function of $|\Theta|$. Also shown is the growth rate γ as a function of $|\Theta|$. The values of γ, $\xi_{\psi 2}/\xi_{\psi 1}$, and $\xi_{\psi 3}/\xi_{\psi 1}$ for a uniform, continuous wall (at left; solid) and with no wall (at right; solid) are also shown, as are the $\xi_{\psi 2}/\xi_{\psi 1}$ and $\xi_{\psi 3}/\xi_{\psi 1}$ ratios for the Fourier representation of the uniform vertical rigid shift (on the axis) for comparison.

The results show that the most effective stabilizing position for the plates is directly above and below the plasma at $|\Theta| = \pi/2$. The growth rate rises rapidly as the conductors are moved away from this center position. It is interesting to note that the highest growth rate, corresponding to the case in which the plates are adjacent at the inboard midplane, is nearly as large as the growth rate with no passive stabilization whatsoever. In fact, this point and the neighboring positions are ideally unstable, i.e., unstable with ideal conductors. The vertical lines mark the ideal stability boundaries. The points outside the region bounded by these lines re ideally unstable. It is clear that conductors located on the far outboard or inboard sides provide very little stabilization. There is, however, a well defined minimum in the growth rate for the plates located at $|\Theta| = \pi/2$, where

the growth rate is only about 3.5 times that for a completely enclosing wall. Therefore, optimally placed conductors can provide much stabilization.

The form of ξ_ψ for the purely vertical rigid shift is essentially identical to the true eigenfunction with no wall. This is also very similar to the eigenfunction with a completely enclosing resistive wall. But when discrete passive conductors are present, and are moved in poloidal position, the resulting eigenfunctions vary significantly from a rigid shift.

The relative contribution of the $m = 2, 3$ components to the eigenfunction is seen to vary considerably as the plate position is varied, with the $m = 2$ contribution dominating the $m = 3$ contribution by as much as a factor of 4. It is interesting that for the cases with either a completely surrounding resistive wall, or no wall at all, the $m = 2$ contribution is nearly zero, and the $m = 3$ component is the only significant higher m contribution to the eigenfunction. Also, the $m = 2$ contribution is zero when the plates are placed at $|\Theta| = \pi/2$. Therefore it is only for off-center placement of the discrete conductors that we see any $m = 2$ contribution. It is also seen that the variations in the eigenfunction and growth rate are almost completely symmetric (or antisymmetric) with respect to $|\Theta| = \pi/2$. We show in the following sections that the curves for γ, $\xi_{\psi 2}/\xi_{\psi 1}$, and $\xi_{\psi 3}/\xi_{\psi 1}$ exhibit less symmetry with respect to $|\Theta| = \pi/2$ for equilibria with lower aspect ratio and especially for those with triangularity.

Let us now consider the variations in the relative magnitudes of the $m = 2$ and $m = 3$ components of the eigenfunction. The induced currents in a resistive conductor that passively stabilizes the plasma are proportional to the magnitude of the perturbed poloidal flux that diffuses through the conductor. In the thin-wall approximation this is reflected in the jump condition [25] at the resistive wall, Eq. 9. Figure 2a,b shows the perturbed flux, for the large aspect ratio elliptical equilibrium surrounded by a uniform, continuous resistive wall, due only to the $m = 2$ and $m = 3$ components of the eigenfunction, respectively. The signs of these components of the perturbed flux with respect to the dominant $m = 1$ component are also shown.

The $m = 1$ component of the eigenfunction always dominates and therefore accounts for the largest part of the stabilizing wall currents. In certain regions the perturbed flux due to one of the $m > 1$ components of the eigenfunction is of the opposite sign to the flux from the dominant $m = 1$ component. Therefore, the eddy currents induced by these higher m components of the flux subtract from the overall stabilizing eddy currents for conductors in those regions. In other regions these components of the flux are of the same sign as the dominant $m = 1$ component to the flux and therefore they add to the stabilizing effect. Clearly an increase in one of the $m > 1$ components would enhance the stabilizing effect of a conductor which is present in the region where this component of the flux has the same sign at the $m = 1$ component, but would detract from the stabilizing effect when it is in a region of the opposite sign flux. For this simple case the m^{th} poloidal harmonic component of the flux divides each half plane into m regions of roughly equal extent in Θ and of alternating sign.

If we examine the variation in $\xi_{\psi 2}/\xi_{\psi 1}$ in Fig. 1 and compare to Fig. 2a we see that when the conductor is in the region where a positive $\xi_{\psi 2}/\xi_{\psi 1}$ would induce positive wall currents the ratio $\xi_{\psi 2}/\xi_{\psi 1}$ is, in fact, negative. Conversely, when the conductor is in the other region of the half-plane (where a positive $\xi_{\psi 2}/\xi_{\psi 1}$ induces a negative contribution to the wall currents) the ratio $\xi_{\psi 2}/\xi_{\psi 1}$ is positive. So we see that the $m = 2$ contribution to the induced currents in the conductor always reduces the total induced current and is thereby destabilizing. Only when the conductors are directly above and below the plasma, centered at $|\Theta| = \pi/2$ where the $m = 2$ component would cancel itself anyway, is this component zero, as it is in the case with no wall or a complete continuous wall.

The variation in $\xi_{\psi 3}/\xi_{\psi 1}$ shows similar behavior. This curve changes sign twice as $|\Theta|$ is varied and this is such that the $m = 3$ component induces destabilizing eddy currents when the discrete conductor is any region. The curve is weighted towards the negative side since the rigid shift eigenfunction has a small, negative $m = 3$ component, but it does become small and positive in the region centered about $|\Theta| = \pi/2$ which induces destabilizing currents in a conductor in that region.

Therefore the growth rate is smallest and the plasma is effectively stabilized on the ideal time scale when the conductors are centered at $|\Theta| = \pi/2$. Here the $m = 2$ contribution is zero, and the $m = 3$ component is destabilizing, but small. As the conductors are moved away from $|\Theta| = \pi/2$ the $m = 2$ component increases rapidly in magnitude and is always destabilizing. These modifications of the eigenfunction lead to vast changes in the growth rate as the conductors are moved in Θ.

The form of the eigenfunction with a uniform surrounding resistive wall reflects the sum of the effects of the conductors at all the poloidal positions along the wall contour. The values for $\xi_{\psi 2}/\xi_{\psi 1}$ and for $\xi_{\psi 3}/\xi_{\psi 1}$ with the complete wall are roughly in the middle of the range of the different points in Fig. 1.

Next we consider toroidal effects by studying a lower aspect-ratio ellipse with $A = 4.5$, and $\kappa = 1.6$. The effect of toroidicity is clearly seen in Fig. 3. These curves show the normalized stabilizing radial field at the magnetic axis, $\vec{b}_r(0)$, due to a unit current at every poloidal position Θ on the wall contour. This is shown for both the low aspect ratio ellipse of Section 3.2 (solid) and for the very large aspect ratio ellipse (dotted). Clearly the currents on the outboard side provide a much more stabilizing effect than those on the inboard side for the low aspect ratio case. We expect, therefore, significantly higher growth rates for conductors on the inboard side compared to outboard conductors for this case. It is interesting to note, however, the dominating effect of the modification of the eigenfunction. For the very large aspect-ratio case, if the conducting plates are centered at either of the two maxima of $\vec{b}_r(0)$ on either side of $|\Theta| = \pi/2$ the growth rate is much higher (by over a factor of 200—i.e., ideally unstable) than for the conductor at $|\Theta| = \pi/2$. This is true even though the stabilizing effect of a unit current is highest at those points. This is due to the large destabilizing contributions from the $m = 2$ and $m = 3$ components of the modified eigenfunction which significantly reduce the overall induced current. These modifications reduce the stabilizing currents to such an extent that passive conductors at these positions are ineffective in spite of the slight advantage in $\vec{b}_r(0)$.

3.2. *A lower aspect-ratio elliptical equilibrium*

We perform this study again with an elliptical plasma at lower aspect ratio ($A = 4.5$). The equilibrium parameters such as physical dimension, elongation, and toroidal field are the same as the for ARIES-I equilibrium [27–29] but the triangularity is zero. We can compare the results of this case to the previous case in order to see how toroidal effects come into play.

Shown in Fig. 4 are the Fourier components for the true eigenfunction for the case of a completely surrounding conducting wall (Fig. 4a) and for the uniform vertical rigid shift (Fig. 4b). The form of the components for the actual eigenfunction and the rigid shift are very similar, indicating that the most unstable displacement when a full wall is present is, in fact, very nearly a uniform rigid shift. Nevertheless, we see from Fig. 5 that the form of the eigenfunction changes significantly with respect to the position of the plates, and thus shows some deformability and variance from the rigid shift. Figure 5 also shows how the growth rate γ varies with respect to poloidal plate position.

The form of the curves in Fig. 5 is noticeably different from the very large aspect-ratio case, Fig. 1. The curves in this case are less symmetric about $|\Theta| = \pi/2$, which is a consequence of toroidal effects. The optimal plate position for passive stability is now slightly towards the outboard side at about $|\Theta| = 0.448\pi$. The points on the outboard side ($\Theta < \pi/2$) have significantly lower growth rates than their corresponding points on the inboard side. The $\xi_{\psi 2}/\xi_{\psi 1}$ curve is no longer symmetric about $\xi_{\psi 2}/\xi_{\psi 1} = 0$. The value of $\xi_{\psi 2}/\xi_{\psi 1}$ at $|\Theta| = \pi/2$ is approximately 0.1, which is very close to the values both for the case with a complete resistive wall and for the case with no wall. Thus we see that the $\xi_{\psi 2}/\xi_{\psi 1}$ values are shifted towards the positive. It is interesting to note that the point where $\xi_{\psi 2}/\xi_{\psi 1}$ crosses zero has roughly the lowest growth rate (this was also true in the large aspect ratio case) indicating that a nonzero $m = 2$ component is destabilizing. The $\xi_{\psi 3}/\xi_{\psi 1}$ curve is also shifted far to the positive side, and is no longer symmetric with respect to $|\Theta| = \pi/2$. The vertical lines in Fig. 5 again show the ideal stability

boundaries. This region is no longer symmetric with respect to $|\Theta| = \pi/2$, but is shifted slightly to the outboard side which reflects the toroidal effects.

We again see that the eigenfunction is modified by the position of the conductor in such a way that the $m = 2, 3$ components change to reduce their contribution to the stabilizing eddy currents for each configuration of passive plates. When the poloidal plates are in the outboard region the eigenfunction is such that the $m = 2$ component is negative and therefore destabilizing. As the plates are positioned in the inboard region the $m = 2$ component becomes positive, which is strongly destabilizing for conductors in this region. Also, while the $m = 3$ component never becomes negative, it does vary greatly in magnitude with respect to the plate position in order to weaken the stabilizing influence of the plates.

An explicit demonstration of the plasma deformation is presented in Figs. 6 and 7. The figures show the Fourier decomposition of the radial eigenfunction ξ_ψ and the projection of the displacement $\vec{\xi}$ onto the poloidal plane for the case of the plates on the inboard side $|\Theta| \approx 3\pi/4$ (Fig. 6) and on the outboard side at $|\Theta| \approx \pi/4$ (Fig. 7). It is seen that the unstable plasma displacement adjusts as the plates are moved so that the stabilizing effect of the plates is reduced.

Figure 6a shows the eigenfunction ξ_ψ for the case with the passive plates on the inboard side at $|\Theta| \approx 3\pi/4$ (second point from the right on the curves in Fig. 5). The eigenfunction ξ_ψ is noticeably different from the eigenfunction for the case with a full wall and also from the rigid displacement. The differences result in the plasma displacement shown in Fig. 6b in which the displacement is seen to be small on the inboard side near the plates, and is such that the displacement normal to the conducting plates is reduced near the plates. In this way the plasma appears to "slip" around the plates in a way to reduce the resistance to the motion.

Figure 7 shows the eigenfunction of the instability with the passive plates on the outboard side at $|\Theta| \approx \pi/4$ (second point from the left on the curves in Fig. 5). The

Plasma Current I_p	12.30 MA
Major Radius R_0	2.182 m
Minor Radius a	0.660 m
Elongation $\kappa(95\%)$	1.996
Triangularity $\delta(95\%)$	0.258
Toroidal Field $B_T(0)$	11.0 T
$q(95\%)$	4.5
β	0.0092
$n_e(0)$	1.08×10^{21} m^{-3}

Table 1: Equilibrium parameters of CIT plasma used in the passive stabilization study.

deformation of the eigenfunction is clearly different from that of Fig. 6, and it is again quite different from the rigid shift. This difference can be traced to a change in magnitude of the $m = 3$ component and a change in sign and magnitude of the $m = 2$ component. The displacement vector plot shows the plasma is again displaced in such a way that the stabilizing effect of the plates is reduced. The magnitude of the displacement is seen to be very small on the outboard side near the plates, and the displacement normal to the conductors is reduced which causes reduced stabilization from the plates.

3.3. *The CIT equilibrium*

We now perform the same study using the CIT design equilibrium. This equilibrium has been studied in depth using the NOVA-W code with regard to convergence studies and active feedback stabilization [25]. The equilibrium parameters are shown in Table 1. This equilibrium has significant triangularity ($\delta = 0.26$) as well as elongation ($\kappa = 2.0$). We study the variations in the growth rate and the relative non-rigid component contributions

to the eigenfunction with respect to the position of the symmetric poloidal plates as was done in the previous sections. The results are shown in Fig. 8, in the same fashion as the results of previous two cases.

The same reasoning can be applied to the variations in the relative contributions $\xi_{\psi m}/\xi_{\psi 1}$ for this equilibrium. Figure 9 shows the contributions of the $m = 2$ and $m = 3$ components to the perturbed flux in the vacuum. We note that the $\xi_{\psi 2}/\xi_{\psi 1}$ ratio in Fig. 8 changes sign as the conducting plates are moved from the outboard region to the inboard region, so that the $m = 2$ contribution to the eddy currents in the conductors is always of opposite sign to the overall stabilizing currents. However, the maximum positive magnitude is over twice as large as the maximum negative magnitude. This reflects the significant $m = 2$ component to the eigenfunction in the case with no conductors. The $m = 3$ component to the eigenfunction doesn't change sign like the $m = 2$ component, however its magnitude is much higher when the conductors are in the region in which the $m = 3$ component adds negatively to the overall eddy currents. It varies with respect to the position of the conductors to increase its destabilizing contribution and decrease its stabilizing contribution.

The eigenfunction for this equilibrium with significant triangularity (both with a complete wall and with no wall) is quite different from the uniform vertical rigid shift. The displacement has a prominent inward motion towards the $\times$-point region [25]. For the configurations with the conductors on the outboard side this effect is enhanced and the eigenfunction differs even further from a rigid shift. However, when the conductors are on the inboard side this effect is reduced and the most unstable motion for this case is, in fact, nearly a uniform, vertical shift. Both cases show the effect of the placement of the passive conductors to modify the eigenfunction such that the motion towards the conductors is reduced.

The effect of triangularity in this equilibrium makes the curves in Fig. 8 even less symmetric with respect to $|\Theta| = \pi/2$ than the previous case. The most effective plate

position is further to the outboard side at about $|\Theta| = 0.403\pi$. The vertical lines show the ideal stability boundaries, and it is seen that all configurations with the plates centered on the inboard side are ideally unstable. The region in which passive conductors give ideal stability is narrower than the previous cases and is exclusively on the outboard side, basically limited to $\pi/4 \leq |\Theta| \leq \pi/2$.

This analysis has also been performed for the ARIES-I design equilibrium [26]. This equilibrium has a smaller elongation ($\kappa = 1.61$), but larger triangularity ($\delta = 0.43$), than the CIT design equilibrium. The eigenfunction is much further from a uniform, vertical shift than the previous case, again even more so when the conductors are on the outboard side, but again to a lesser extent when the conductors are on the inboard side. The greater triangularity of this equilibrium eliminates even further any symmetry about $|\Theta| = \pi/2$, and the most effective conductor position is slightly further to the outboard side at about $|\Theta| = 0.394\pi$. This is true even though the ARIES-I equilibrium has a larger aspect ratio than the CIT equilibrium. This indicates that triangularity leads to preferred outboard positions of the conductors to an even greater extent than toroidal effects.

A similar analysis, but one which used a rigid plasma motion assumption, has been carried out for the ITER configuration [13]. In this case a comparison was made between growth rates with a full wall and a partial wall covering about half the area on the outboard side. It was shown that an optimally placed partial wall would stabilize the plasma almost as well as a complete wall—the partial wall growth time being higher by an average factor of only 1.6 times the full wall growth rate. Another study for the ARIES-I reactor design [29] gave similar results with this rigid plasma model. It was also shown that the growth rate for ARIES-I with a full wall using the rigid plasma model was 20% lower than the result from NOVA-W. In general, we see that stabilization by a partial wall will be much less effective because of deformations in the plasma eigenfunction. Clearly plasma deformations can play a significant role in the passive stabilization of highly shaped tokamak plasmas.

Plasma Current I_p	567.4 kA
Major Radius R_0	1.635 m
Minor Radius a	0.308 m
Elongation $\kappa(95\%)$	1.951
Toroidal Field $B_T(0)$	1.20 T
$q(95\%)$	2.51
β	0.02
$n_e(0)$	3.35×10^{19} m^{-3}

Table 2: Equilibrium parameters of PBX-M plasma used in the active feedback stabilization study. This equilibrium corresponds to a modification of the equilibrium of experimental shot #226879.

4. Non-rigid effects on the active feedback stabilization of PBX-M

In this section we consider the effects of an active feedback system on the form of the eigenfunction and how this affects the overall stability. In Ref. [23] a numerical calculation using the Tokamak Simulation Code [18] of the active feedback stabilization of the axisymmetric instability in the PBX-M tokamak was described. It was demonstrated that different flux-loop locations which measure equally well the plasma displacement in the passive sense do not work equally well in stabilizing the axisymmetric motion given the same active feedback coils and gain law. In particular, it was shown that the flux loop pair on the inboard side was ineffective in stabilizing the vertical instability regardless of the value of the gain. The outboard pair, however, could be used successfully to stabilize the plasma.

These results were demonstrated using Nyquist techniques, and it was suggested that if the plasma were unstable enough, it would be able to deform under the influence of the active feedback (i.e., the eigenfunction would be modified) which in such a way that the flux difference measurement at the flux loops could be made so close to zero that the active feedback system would be rendered ineffective. The feedback system would operate normally, but the flux-loop measurements would be worthless owing to the plasma deformation. It was impossible, however, to explicitly demonstrate this conjecture using TSC and the other analysis methods used. The NOVA-W code, on the other hand, is ideally suited for examining this problem, and we will show how the active feedback system can induce a modification of the PBX-M eigenfunction in such a way as to make the active feedback system ineffective for certain flux-loop locations, and how it will minimize the stabilizing effect of the feedback system for any flux-loop configuration. For this we consider a PBX-M equilibrium similar to that used in Ref. [23].

4.1. *Active feedback stabilization of PBX-M using the inboard flux loops*

We use a PBX-M equilibrium corresponding to experimental shot #226879. The equilibrium parameters are listed in Table 2. The equilibrium used here was taken from a time-dependent TSC simulation in which the actual experimental coil currents from this shot were used for the simulation, and the TSC results compared well with the experimental magnetics data [30]. This was done in the same fashion as an earlier study of the PBX tokamak [17]. To produce the modified equilibrium used in these calculations, the vertical field was increased in order to move the plasma inward, away from the outboard stabilizing plates and toward higher negative field index. This makes the equilibrium more vertically unstable than the original experimental equilibrium. Such an inward radial shift could be caused in an experiment by a loss of thermal energy or redistribution of current [17].

Figure 10 shows the equilibrium plasma boundary, the PBX-M wall contour (the

wall contour is composed of sections of high conductivity which represent the passive stabilizing plates used in the PBX-M device and includes connecting regions of very high resistivity representing the axisymmetric gaps between the passive stabilizers), the active feedback coils, and the three sets of flux loops to be used. We consider first the case of the inboard flux loops, $(X_o, Z_o) = (1.255, \pm 0.10)$, which were found previously [23] to be ineffective for active feedback stabilization. A proportional gain law was used in this calculation. The normalized feedback gain is equal to $\mu_0/2$ times the gain given in units of Amps/Weber-radian.

Figure 11 shows the instability growth rate vs. normalized feedback gain, and selected component ratios ($\xi_{\psi 2}/\xi_{\psi 1}$ and $\xi_{\psi 4}/\xi_{\psi 1}$) vs. gain. As the feedback gain is increased from zero, the growth rate drops rapidly, indicating that the feedback system is operating properly. The components of the eigenfunction remain fairly constant with respect to the gain. At higher gain (approximately $\alpha \geq 1.5$), however, we see that the $m = 2$ component of the eigenfunction changes significantly. It becomes less negative, then positive, and then rapidly increases in magnitude with increasing gain. In the same region of gain space where we see the sudden rapid increase of $\xi_{\psi 2}/\xi_{\psi 1}$ we also notice that the growth rate γ starts to level off. The growth rate approaches marginal stability and does not appear to become more stable at high values of feedback gain. At $\alpha_g = 6.0$, double the maximum gain shown in Fig. 11, the growth rate is still at marginal stability. It is virtually unchanged (only very slightly smaller) from the gain at $\alpha_g = 3.0$. At these high values of gain the active feedback is no longer effective in providing additional stabilization to the plasma. Instead, the eigenfunction is changing in form, thereby maintaining the instability. The ratio $\xi_{\psi 4}/\xi_{\psi 1}$ also changes significantly as the feedback gain is increased—it roughly quadruples in magnitude in this range of the feedback gain.

Figures 12–14 show the perturbed flux contour plots at three different values of normalized gain ($\alpha_g = 1.0, 2.0, 3.0$) spanning the range of Fig. 11. Examining these perturbed flux plots allows us to see how the eigenfunction modification changes the effectiveness of the feedback system which uses the inboard flux loops.

Figure 12 shows the perturbed flux contours with normalized gain $\alpha_g = 1.0$. Referring to Fig. 11 we see that the eigenfunction is nearly identical to the form it takes with no active feedback—the ratio $\xi_{\psi 2}/\xi_{\psi 1}$ is virtually unchanged, and $\xi_{\psi 4}/\xi_{\psi 1}$ is only slightly more negative. Therefore Fig. 12 shows, in effect, a plot of the perturbed flux contours of the feedback system interacting with essentially the original unstable eigenfunction. We see that the perturbed flux contours from the plasma are fairly equally weighted on both sides of the plasma. The zero contour, shown as a dotted line on this diagram, is distant from the flux loops, and the value of the perturbed flux at the flux loops (measurable signal) is relatively large.

Figure 13 shows the perturbed flux contours for $\alpha_g = 2.0$. Referring to Fig. 11 we see that the eigenfunction has undergone considerable modification at this value of gain. In particular, the $m = 2$ component is quite different and has even changed sign. One can see from the plot of the perturbed flux contours that the contours of plasma flux have become shifted toward the outboard side, and the value of perturbed flux on the inboard side near the flux loops has been greatly reduced. The null contour has moved closer to the flux loops. We see from Fig. 11 that at this point the growth rate has already begun to level off with respect to increasing feedback gain. The change in the form of the perturbed flux contours from the plasma indicates a shift in the unstable plasma motion toward the outboard side.

Figure 14 shows the perturbed flux contours when the normalized gain $\alpha_g = 3.0$, the highest gain value shown in Fig. 11. The plasma deformation is quite large at this point, especially with regard to the $m = 2$ component. The perturbed flux contours also reflect the considerable deformation of the plasma. The contours from the plasma are heavily weighted toward the outboard side. The perturbed flux indicates that the unstable motion is now more of a purely vertical motion instead of the motion towards the $\times$-point (in the direction of the tip of the bean) which is characteristic of the instability with little or no active feedback—see Fig. 12. Notice also that the perturbed flux on the inboard side, near the flux loops, is almost zero. There are no contours of plasma flux

seen on the inboard side, and the deformation of the eigenfunction has allowed the null contour to move very close to the flux loops. The measured flux difference at the flux loops is now very small. The feedback system is rendered ineffective because it can no longer measure and feed-back on the deformed vertical motion.

It should be noted that although the case we examined in this section had zero derivative gain, an increase in the derivative gain was found to have no real effect on the stabilization. The growth rate at large gain α_g is still at the marginal stability limit with increased derivative gain. This is not surprising, since the results show the oscillation frequency ω_r to be zero. Therefore there is no overshoot and no oscillation. The ineffectiveness of the feedback using these flux loops is due solely to the eigenfunction deformation.

4.2. Active feedback stabilization using the centered-outboard flux loops

We next consider feedback stabilization using the centered-outboard pair of flux loops of Fig. 10, $(X_o, Z_o) = (1.64, \pm.56)$. This flux-loop pair location corresponds most closely to the actual flux loops used for vertical control in the PBX-M experiment. Figure 15a shows the growth rates vs. proportional gain α_g for three different values of derivative gain β_g. Figure 15b shows the growth rate γ vs. oscillation frequency ω_r for the same three values of derivative gain. It can be seen that with zero derivative gain the axisymmetric mode cannot be stabilized. The growth rate can be reduced to about 20 s^{-1} at $\alpha_g = 1.5$, but further increases in gain do not appreciably lower the growth rate while they do however, significantly increase the oscillation frequency ω_r. Large proportional gain is driving a large overshoot that leads these to oscillations. Clearly some derivative gain is necessary. By increasing the derivative gain to $\beta_g/\alpha_g = 0.05s^{-1}$ the plasma can be stabilized and the oscillations significantly reduced. A further increase in derivative gain to $\beta_g/\alpha_g = 0.10s^{-1}$ decreases the oscillation frequency even more and allows stabilization to occur at a lower value of proportional feedback. Unlike the inboard flux-loop pair,

this pair of flux loops does allow for adequate stabilization of the plasma provided the derivative gain is large enough. This agrees with results obtained with TSC for this same equilibrium [30]. Figure 16 shows the variation of the $m = 2, 4$ components of the eigenfunction, as well as the growth rate γ and oscillation frequency ω_r, with respect to feedback gain α_g for the three values of derivative gain.

Figure 16a shows these results for the case with no derivative gain. We see a strong reduction in the growth rate γ with increasing gain α_g until the gain reaches $\alpha_g \approx 1.5$. At this point the γ curve levels off and does not stabilize much more with further increase in gain. Furthermore, we see ω_r increase rapidly from zero beginning at $\alpha_g \approx 1.25$. The oscillation frequency ω_r increases steadily with increasing gain, while γ no longer decreases by any significant amount. This demonstrates that the restoring force from the feedback system is driving the oscillations instead of stabilizing the plasma. We also see some modification of the $m = 2, 4$ components of the eigenfunction in Fig. 16a. This deformation, while noticeable, is not strong at this point.

Figure 16b shows the results for the case using the centered-outboard flux loops with $\beta_g/\alpha_g = 0.05\text{s}^{-1}$ derivative gain. In this case the plasma can be stabilized with sufficiently large feedback gain. The oscillation frequency here is less than that in the zero derivative gain case, although it is still a significant fraction of that case and continues to increase with increasing gain. We also see a larger change in $\xi_{\psi 2}/\xi_{\psi 1}$ with respect to increasing gain α_g than in the zero derivative gain case. After a small decrease in negative magnitude at $\alpha_g \approx 0.75$, the value of $\xi_{\psi 2}/\xi_{\psi 1}$ begins to get more negative with increasing gain. This change in $\xi_{\psi 2}/\xi_{\psi 1}$ corresponds to a change in the slope of the γ vs. α_g curve. As $\xi_{\psi 2}/\xi_{\psi 1}$ begins to become more negative, the reduction in γ with respect to α_g decreases. Thus, there appears to be a plasma deformation that is reducing the effectiveness of the feedback system with the flux loops at this location. This modification is not enough to keep the feedback system from stabilizing the vertical instability, but it does reduce the effectiveness as shown by the change in slope of the γ vs. α_g curve.

Finally, Fig. 16c shows the results for the case with $\beta_g/\alpha_g = 0.10\text{s}^{-1}$ derivative gain. In this case the oscillations have been much reduced, and the plasma is stabilized at a lower value of α_g. Here also, we see a large change in $\xi_{\psi 2}/\xi_{\psi 1}$ with respect to the gain. There is a rapid decrease in $\xi_{\psi 2}/\xi_{\psi 1}$ with respect to α_g starting at $\alpha_g \approx 0.75$. This is strongly correlated with the sudden change in the slope of the γ vs. α_g curve. The γ vs. α_g curve levels off in the region where the eigenfunction is significantly deformed. This corresponds to about the point where the axisymmetric mode becomes stable, so the deformation is not enough to keep the plasma unstable when these flux loops are used, but it does keep the feedback system from stabilizing the motion any further, as witnessed by the sudden change in slope of the γ vs. α_g curve.

The $m = 2$ component ratio $\xi_{\psi 2}/\xi_{\psi 1}$ begins to decrease (increase in negative magnitude) as the gain is increased above $\alpha_g \approx 1.0$–1.5. Note that this change is opposite to the change in $\xi_{\psi 2}/\xi_{\psi 1}$ from Fig. 11 for the inboard flux loops. In that case we found that $\xi_{\psi 2}/\xi_{\psi 1}$ changed sign and grew to a large (positive) value with increasing feedback gain. This caused the perturbed flux contours from the plasma to be shifted toward the outboard side away from the flux loops. This left a relatively small value of perturbed plasma flux at the inboard flux loops. In the present case, when the centered-outboard flux loops are used to control the feedback system, we see the opposite effect. This implies that the perturbed flux on the outboard region near these flux loops is somewhat reduced.

Figure 17 shows the perturbed flux contours for the active feedback at gain $\alpha_g = 2.25$ using the centered-outboard flux loops. Careful examination and comparison with Fig. 12 shows that the perturbed flux near the flux loops is slightly reduced from the case with little or no feedback gain. This is most clear by noticing how much closer the zero-flux contour has moved to the controlling pair of flux loops. The plasma eigenfunction is again deformed in such a way to reduce the effectiveness of the feedback system using this particular pair of flux loops. However, the deformation is clearly very different from the inboard flux-loop case as one can see by the difference in $\xi_{\psi 2}/\xi_{\psi 1}$ vs. α_g in Figs. 11 and

16. This results in a quite different modification of the perturbed flux contours between Figs. 14 and 17. The only difference between these two cases is the location of the flux loops, and this difference leads to vastly different plasma deformations.

It is interesting that the deformation is weak when the feedback system is ineffective due to insufficient derivative gain. However, as the derivative gain is increased, thereby reducing the unwanted oscillations, the feedback is more effective in reducing the growth rate, but it is also more effective at inducing a deformation in the eigenfunction. This deformation becomes larger with increasing gain, and the effectiveness of the feedback system is reduced.

4.3. Active feedback stabilization using the far-outboard flux loops

Next we consider active feedback using the far-outboard flux loops shown in Fig. 10. Figure 18 shows the results using this pair of flux loops with a gain law that includes derivative gain of $\beta_g/\alpha_g = 0.10\text{s}^{-1}$. We see that even with this large derivative gain and the correspondingly low values of ω_r shown in Fig. 18, the plasma cannot be stabilized beyond a certain point ($\gamma \approx 4\ \text{s}^{-1}$). Figure 18 shows a large initial drop in γ with increasing gain. This stabilization begins to level off, however, at $\alpha_g \approx 1.75$.

The component ratios $\xi_{\psi 2}/\xi_{\psi 1}$ and $\xi_{\psi 4}/\xi_{\psi 1}$ show a significant and varied deformation of the eigenfunction with respect to increasing gain. Initially there is a sharp rise in $\xi_{\psi 2}/\xi_{\psi 1}$ toward less negative values. This mimics the rapid rise in $\xi_{\psi 2}/\xi_{\psi 1}$ shown in Fig. 11 for the case using the inboard flux loops. In that case, however, $\xi_{\psi 2}/\xi_{\psi 1}$ moves to positive values and continues to increase in magnitude. In Fig. 18 we see such an initial rise in $\xi_{\psi 2}/\xi_{\psi 1}$, but then a sharp reversal occurs at $\alpha_g \approx 1.75$, followed by a rapid decrease of $\xi_{\psi 2}/\xi_{\psi 1}$ (toward more negative values) at higher gain. This is paralleled by a similar, but much less dramatic, change in $\xi_{\psi 4}/\xi_{\psi 1}$ at about the same point. The γ vs. α_g curve levels off at $\alpha_g \approx 1.75$, near the point where we see the sudden changes in the eigenfunction.

Figure 19 shows the perturbed flux contours for this case with the gain $\alpha_g = 2.0$ and the derivative gain $\beta_g/\alpha_g = 0.10\text{s}^{-1}$. We see from this figure that the null contour lies almost directly on the flux loops. This seems to be a natural consequence of the geometry of the feedback system and this particular inward-shifted equilibrium. Note from Fig. 12 (inboard flux loops, gain $\alpha_g = 1.0$) that the null contour on the outboard side is in about the same place even when the flux loops are on the inboard side. However, in the case using the inboard flux loops, we see that at higher values of gain the eigenfunction deformation is such that the perturbed flux contours are shifted strongly toward the outboard side. This, in turn, pushes the null contour away from the plasma.

If this same deformation of the eigenfunction were to occur when the flux loops are on the outboard side of the plasma, then the feedback system would be more effective owing to the large measurable perturbed plasma flux at the flux-loop locations (see Figs. 13–14). What we do see when the flux loops are on the outboard side is a deformation initially similar to the previous case, but then there is a sudden reversal in the plasma deformation at the point where continued deformation would move the null contour away from the flux loops. Instead, the eigenfunction is modified so as to keep the null contour on the flux loops and thereby reduce the stabilizing effect of the feedback system.

5. Summary

For the case of passive stabilization, we have seen that different m-components of the eigenfunction induce different poloidal current distributions in a surrounding wall. Conducting elements at different locations around the plasma will induce differing modifications of these non-rigid components of the eigenfunction. The eigenfunction is modified to either increase the relative magnitude of the $m > 1$ components if they induce destabilizing currents for a particular conductor, or to decrease them if they are stabilizing. Therefore the plasma motion is modified in such a way that it can "slip" around the passive conductors in order to reduce the resistance to its motion. A more precise way

to state this is to say that the plasma eigenfunction is modified in such a way that the stabilizing eddy currents in the surrounding conductors are reduced as much as possible. Toroidal effects remove the symmetry with respect to $|\Theta| = \pi/2$ and push the most effective position for passive conductors to the outboard side. Triangularity removes the symmetry even further and gives even greater advantage to outboard positioning of conductors. In general, effects due to plasma shaping and deformability of the eigenfunction are over and above the relative advantage of placing conductors on the outboard side due to toroidal effects. Therefore, the optimal placement of the discrete conducting plates can be of critical importance for a shaped tokamak plasma.

We have also seen in Section 4 that the eigenfunction of the axisymmetric mode for the PBX-M plasma will modify itself under the influence of an active feedback system to provide a much weaker signal to the flux loops that measure the plasma displacement. This compromises the stabilizing effect of the active feedback system, and can in some cases leave the feedback system so ineffective that stability cannot be achieved regardless of the strength of the feedback gain. We examined, in particular, three possible locations for placement of the flux loops that control the feedback, and in each case we see a different plasma deformation that leads to a reduced flux signal for each particular pair of flux loops. These eigenfunction deformations do not leave the plasma unstable in every case, but they always do reduce the stabilizing effect of the particular feedback configuration.

Note that for all three active feedback cases, the perturbed flux contour plots show that the eigenfunction is modified in such a way that the zero-flux contour is pushed toward the particular set of controlling flux loops. This reflects the reduction in the measurable signal at the flux loops, and thereby the reduction in the effectiveness of a feedback system to control the unstable motion.

We have shown that effects due to the deformability of the plasma can therefore play an important role in determining the properties of passive and active feedback stabiliza-

tion of highly shaped tokamak plasmas. This should be an important consideration in the future design and operation of such tokamaks.

Acknowledgments

The authors would like to thank Dr. N. Pomphrey, Dr. G. H. Neilson, and Dr. C. Kessel for many helpful discussions. This work was supported by U.S. DoE Contract DE-AC02-76CHO3073 and by EURATOM, the Ecole Polytechnique Fédérale de Lausanne, and the Fonds National Suisse de la Recherche Scientifique.

References

[1] Troyon, F., Gruber, R., Saurenmann, H., Semenzato, S., and Succi, S., Plasma Phys. and Contr. Fusion **26** (1984) 209.

[2] Goldston, R. J., Plasma Phys. and Contr. Fusion **26** (1984) 87.

[3] Coppi, B., Dagazian, R., and Gajewski, R., Phys. Fluids **15** (1972) 2405.

[4] Ohkawa, T., and Voorhies, H. G., Phys. Rev. Lett. **22** (1969) 1275.

[5] Lazarus, E. A., Chu, M. S., Ferron, J. R., et al., Phys. Fluids B **3** (1991) 2220.

[6] Pfirsch, D., and Tasso, H., Nucl. Fusion **11** (1971) 259.

[7] Lee, J. K., Nucl. Fusion **26** (1986) 955.

[8] Hofmann, F., Marcus, F. B., and Turnbull, A. D., Plasma Phys. and Contr. Fusion **28** (1986) 705.

[9] Hofmann, F., Turnbull, A. D., and Marcus, F. B., Nucl. Fusion **27** (1987) 743.

[10] Chu, M., Miller, R., and Ohkawa, T., Nucl. Fusion **17** (1977) 465.

[11] Jardin, S. C., Phys. Fluids **21** (1978) 1851.

[12] Dobrott, D., and Chang, C., Nucl. Fusion **21** (1981) 1573.

[13] Leuer, J. A., Fusion Tech. **15** (1989) 489.

[14] Jardin, S. C., and Larrabee, D., Nucl. Fusion **22** (1982) 1095.

[15] Haney, S. W., and Freidberg, J. P., Phys. Fluids B **1** (1989) 1637.

[16] Rebhan, E., and Salat, A., Nucl. Fusion **18** (1978) 1431.

[17] Jardin, S. C., DeLucia, J., Okabayashi, M., et al., Nucl. Fusion **27** (1987) 569.

[18] Jardin, S. C., Pomphrey, N., and DeLucia, J., J. Comp. Phys. **66** (1986) 481.

[19] Lazarus, E. A., Lister, J. B., and Neilson, G. H., Nucl. Fusion **30** (1990) 111.

[20] Lister, J. B., Lazarus, E. A., Kellman, A. G., et al., Nucl. Fusion **30** (1990) 2349.

[21] Grimm, R., Greene, J., and Johnson, J., Computation of the magnetohydrodynamic spectrum in axisymmetric toroidal confinement systems, in J. Killeen, editor, *Methods in Computational Physics, Vol. 16*, pp. 253–280, Academic Press, New York, 1976.

[22] Gruber, R., Troyon, F., Berger, D., et al., Comput. Phys. Commun. **21** (1981) 323.

[23] Pomphrey, N., Jardin, S. C., and Ward, D. J., Nucl. Fusion **29** (1989) 465.

[24] Rosen, M. D., Phys. Fluids **18** (1975) 482.

[25] Ward, D. J., Jardin, S. C., and Cheng, C. Z., Calculation of Axisymmetric Stability of Tokamak Plasmas with Active and Passive Feedback, Report PPPL-2776, Princeton University Plasma Physics Laboratory (July 1991). Submitted to J. Comp. Phys.

[26] Ward, D. J., Studies of Feedback Stabilization of Axisymmetric Modes in Deformable Tokamak Plasmas, PhD Thesis, Princeton Univ., Princeton, NJ (1990).

[27] Najmabadi, F., Conn, R. W., and the ARIES Team, "The ARIES Tokamak Fusion Reactor Study," Proc. IEEE 13th Symp. Fusion Eng., Knoxville, TN (Oct. 1989) 1021.

[28] Conn, R. W., and Najmabadi, F., "Visions of the Future, A Program in Tokamak Reactors Studies," University of California Los Angeles Report UCLA-PPG-1201 (Dec. 1987).

[29] Bathke, C. G., Jardin, S. C., Leuer, J. A., Ward, D. J., and the ARIES Team, Vertical Stability Requirements for the ARIES-I Reactor, Los Alamos Report, LA-UR-89-3327, Los Alamos National Laboratory, Los Alamos (1989)

[30] Ward, D. J., et al., Bull. Am. Phys. Soc. **33** (1988) 2036.

Figures

Fig. 1. Effect of poloidal position $|\Theta|$ of conducting plates on the eigenfunction and growth rate of the very large aspect-ratio elliptical equilibrium. The ratios of the $m = 2$ (circles) and $m = 3$ (triangles) components of the eigenfunction to the $m = 1$ component at the plasma edge are plotted as a function of the poloidal position of the conducting plates. Also shown is the growth rate γ (squares) as a function of the plate position. The corresponding values for a continuous complete wall are shown in solid on the left, and the values for the case with no wall are shown in solid on the right. The values of the ratio $\xi_{\psi m}/\xi_{\psi 1}$ for the Fourier representation of the rigid shift are shown on the left axis. The vertical lines show the ideal stability boundaries, i.e., the configuration is ideally stable when the conductors are located at $|\Theta|$ values in the region between the lines.

Fig. 2. (a) Perturbed flux contour plots for the large aspect ratio ellipse corresponding to the $m = 2$ component of the motion only. The sign of the flux is shown and changes through the midplane and across the zero-flux contours positioned at $|\Theta| = \pi/2$. The midplane itself is also a zero-flux contour.

(b) Perturbed flux contour plots for the large aspect ratio ellipse corresponding to the $m = 3$ component of the motion only. There are two additional zero-flux contours (in addition to the midplane contour, which is always present for antisymmetric modes). The additional zero-flux contours are shown along with the signs (shown in the circles) of the flux contours.

Fig. 3. Magnitude of the perturbed radial magnetic field at the magnetic axis, $\vec{b}_r(0)$, due to a unit (positive) current at every point along the wall contour used in the lower aspect ratio elliptical equilibrium calculation (solid line) and in the very large aspect ratio elliptical equilibrium calculation (dotted line).

Fig. 4. (a) Fourier components of the radial displacement ξ_ψ vs. $\sqrt{\psi}$ for the elliptical

equilibrium with a complete continuous resistive wall.

(b) Fourier components of ξ_ψ for a uniform vertical rigid shift displacement of the elliptical plasma.

Fig. 5. Effect of poloidal position of conducting plates on eigenfunction and growth rate of the lower aspect-ratio elliptical cross-section equilibrium. The ratios of the non-rigid components of the eigenfunction to the rigid component at the plasma edge are graphed as a function of the poloidal position of the conducting plates. In particular the $m = 2$ (circles) and the $m = 3$ (triangles) contributions are shown here. Also shown is the growth rate γ (squares) as a function of the plate position. The corresponding values for a continuous complete wall are shown in solid on the left, and the values for the case with no wall whatsoever are shown in solid on the right. The values of $\xi_{\psi m}/\xi_{\psi 1}$ for the Fourier decomposition of the uniform vertical rigid shift are shown on the left axis. The vertical lines show the ideal stability boundaries.

Fig. 6. (a) Fourier components of the radial displacement ξ_ψ vs. $\sqrt{\psi}$ for the elliptical equilibrium with conducting plates at about 45° off the midplane on the inboard side. (b) Displacement vectors showing the plasma instability. The plasma is partially stabilized by conducting plates on the inboard side of the plasma. Note the deformation of the plasma motion as it tries to move around the plates.

Fig. 7. (a) Fourier components of the radial displacement ξ_ψ vs. $\sqrt{\psi}$ for the elliptical plasma with conducting plates at about 45° off the midplane on the outboard side. (b) Displacement vectors showing the plasma instability. The plasma is partially stabilized by conducting plates on the outboard side of the plasma. Note the deformation of the plasma motion as it tries to move around the plates. Note also the difference in the deformation compared with that of Fig. 6.

Fig. 8. Effect of poloidal position of conducting plates on eigenfunction and growth rate for CIT equilibrium. The ratios of the $m = 2$ (circles) and $m = 3$ (triangles) components of the eigenfunction to the $m = 1$ component at the plasma edge are plotted

as a function of the poloidal position of the conducting plates. Also shown is the growth rate γ (squares) as a function of the plate position. The corresponding values for a continuous complete wall are shown in solid on the left, and the values for the case with no wall are shown in solid on the right. The values of $\xi_{\psi m}/\xi_{\psi 1}$ for the Fourier representation of the uniform vertical rigid shift are shown on the left axis. The vertical lines show the ideal stability boundaries.

Fig. 9. (a) Perturbed flux contour plots for the CIT equilibrium for the $m = 2$ component of the motion. The sign of the flux in each region shown. The midplane is itself a zero-flux (null) contour. This is a $\psi_{\mathbf{rat}} = 0.99$ equilibrium.
(b) Perturbed flux contours for CIT due to the $m = 3$ component of the eigenfunction only. Note the 3-part structure of the contours in each half-plane. The zero-flux contours are indicated with arrows.

Fig. 10. The PBX-M plasma boundary, resistive wall contour, active feedback coils, and three sets of flux observation loops (inboard pair, centered-outboard pair, and far-outboard pair) to be used in these calculations.

Fig. 11. Growth rate γ and variation in $m > 1$ components vs. normalized feedback gain $\alpha_{\mathbf{g}}$ for flux loops on the inboard side. The ratios of the $m = 2$ (circles) and $m = 4$ (triangles) components of the eigenfunction to the $m = 1$ component at the plasma edge are graphed as a function of the feedback gain. Also shown is the growth rate γ (squares) as a function of the gain.

Fig. 12. Perturbed flux contour plots for PBX-M with active feedback using the inboard flux loops, and normalized feedback gain $\alpha_g = 1.0$. The zero-flux contours are shown as dashed lines. The flux loops are shown by '$\times$' symbols.

Fig. 13. Perturbed flux contour plots for PBX-M with active feedback using the inboard flux loops, and normalized feedback gain $\alpha_g = 2.0$. The zero-flux contours are shown as dashed lines. The flux loops are shown by '$\times$' symbols.

Fig. 14. Perturbed flux contour plots for PBX-M with active feedback using the inboard flux loops, and normalized feedback gain $\alpha_g = 3.0$. The zero-flux contours are shown as dashed lines. The flux loops are shown by '×' symbols.

Fig. 15. (a) Growth rate vs. gain α_g for $\beta_g/\alpha_g = 0.$ (squares), $\beta_g/\alpha_g = 0.05\text{s}^{-1}$ (circles), $\beta_g/\alpha_g = 0.10\text{s}^{-1}$ (triangles).
(b) Growth rate vs. $|\omega_r|$ for the same three values of β_g.

Fig. 16. Growth rate γ, oscillation frequency ω_r, and the variation in $m > 1$ components vs. feedback gain for centered-outboard flux loops. The ratios of the $m = 2$ (circles) and $m = 4$ (triangles) components of the eigenfunction to the $m = 1$ component at the plasma edge are graphed as a function of the feedback gain. Also shown is the growth rate γ (squares) and oscillation frequency ω_r (diamonds) as a function of the proportional gain for:
(a) $\beta_g/\alpha_g = 0.$
(b) $\beta_g/\alpha_g = 0.05\text{s}^{-1}$
(c) $\beta_g/\alpha_g = 0.10\text{s}^{-1}$

Fig. 17. Perturbed flux contour plots for PBX-M with active feedback using the centered-outboard flux loops, and normalized feedback gain $\alpha_g = 2.25$. The zero-flux contours are shown as dashed lines. The flux loops are shown by '×' symbols.

Fig. 18. Growth rate γ, oscillation frequency ω_r, and variation in $m > 1$ components vs. feedback gain for far-outboard flux loops. The ratios of the $m = 2$ and $m = 4$ components of the eigenfunction to the $m = 1$ component at the plasma edge are graphed as a function of the feedback gain. Also shown is the growth rate γ and oscillation frequency ω_r as a function of the proportional gain for $\beta_g/\alpha_g = 0.10\text{s}^{-1}$.

Fig. 19. Perturbed flux contour plots for PBX-M with active feedback using the far-outboard flux loops, and normalized feedback gain $\alpha_g = 2$. The zero-flux contours are shown as dashed lines. The flux loops are shown by '×' symbols.

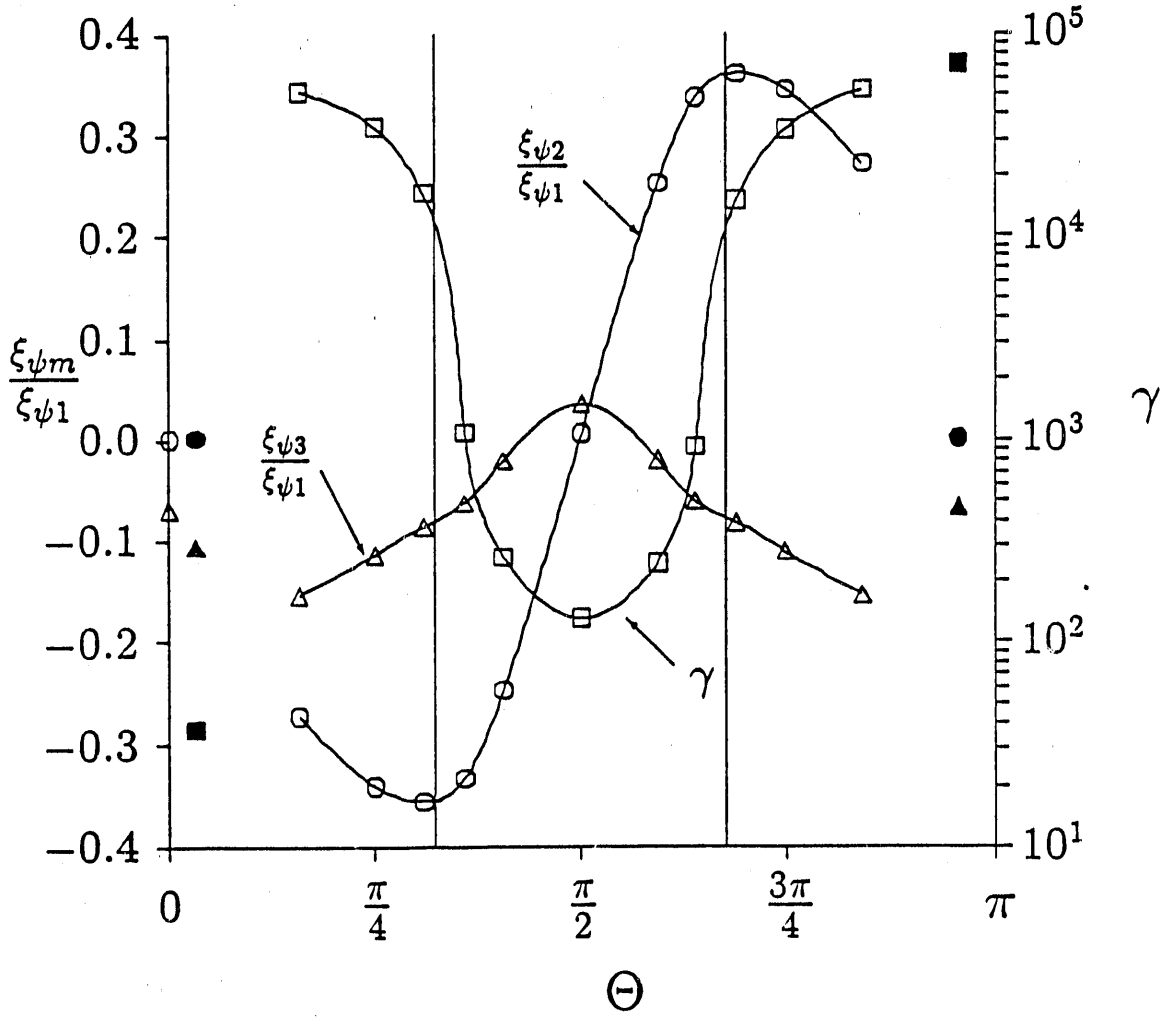
0.4
0.3
0.2
0.1
0.0
−0.1
−0.2
−0.3
−0.4
$\frac{\xi_{\psi m}}{\xi_{\psi 1}}$
10^5
10^4
10^3
10^2
10^1
γ
$\frac{\xi_{\psi 2}}{\xi_{\psi 1}}$
$\frac{\xi_{\psi 3}}{\xi_{\psi 1}}$
γ
0
$\frac{\pi}{4}$
$\frac{\pi}{2}$
$\frac{3\pi}{4}$
π
Θ

Figure 1

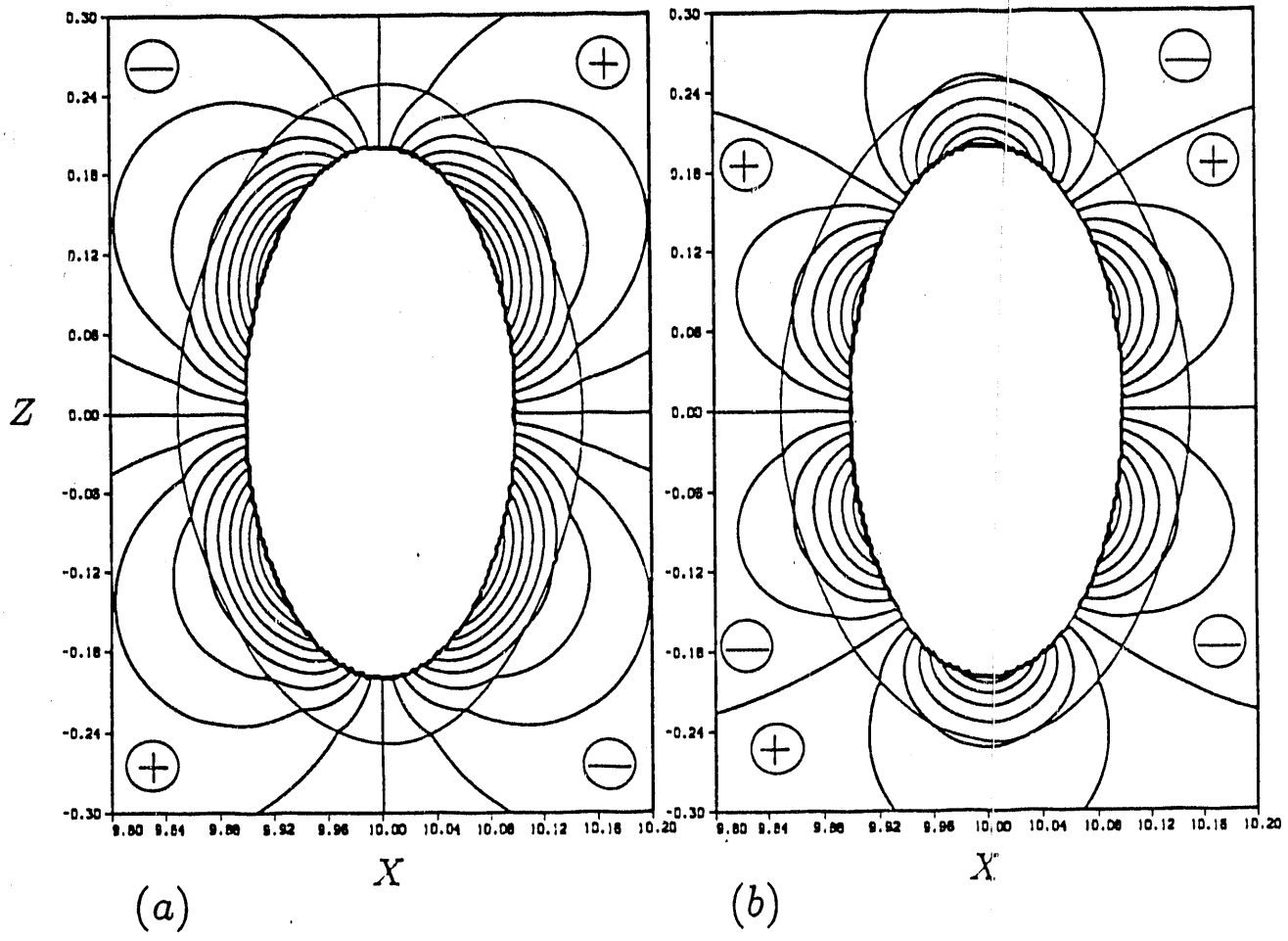
0.30
0.24
0.18
0.12
0.06
0.00
-0.06
-0.12
-0.18
-0.24
-0.30
Z
9.80 9.84 9.88 9.92 9.96 10.00 10.04 10.08 10.12 10.16 10.20
X
(a)
(b)

Figure 2

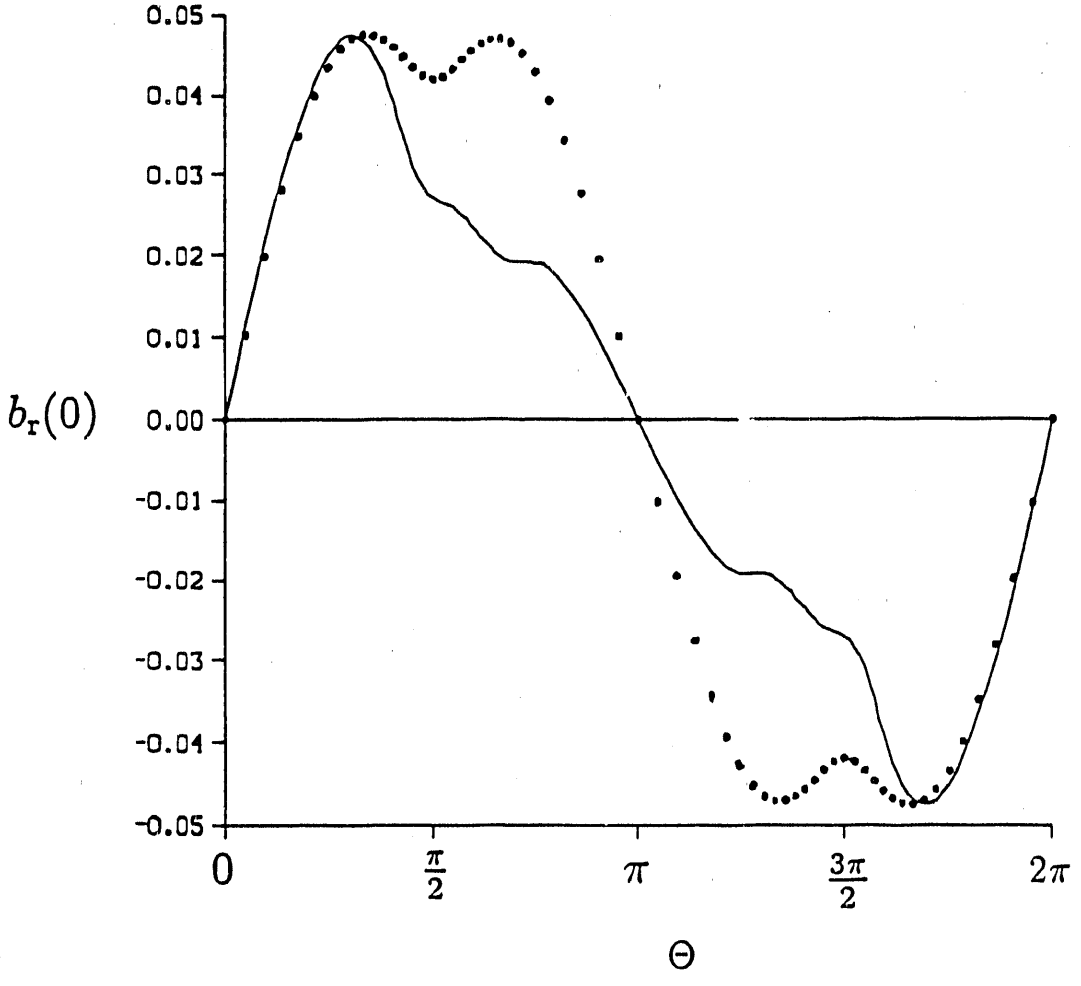
0.05
0.04
0.03
0.02
0.01
0.00
-0.01
-0.02
-0.03
-0.04
-0.05
$b_r(0)$
0
$\frac{\pi}{2}$
π
$\frac{3\pi}{2}$
2π
Θ

Figure 3

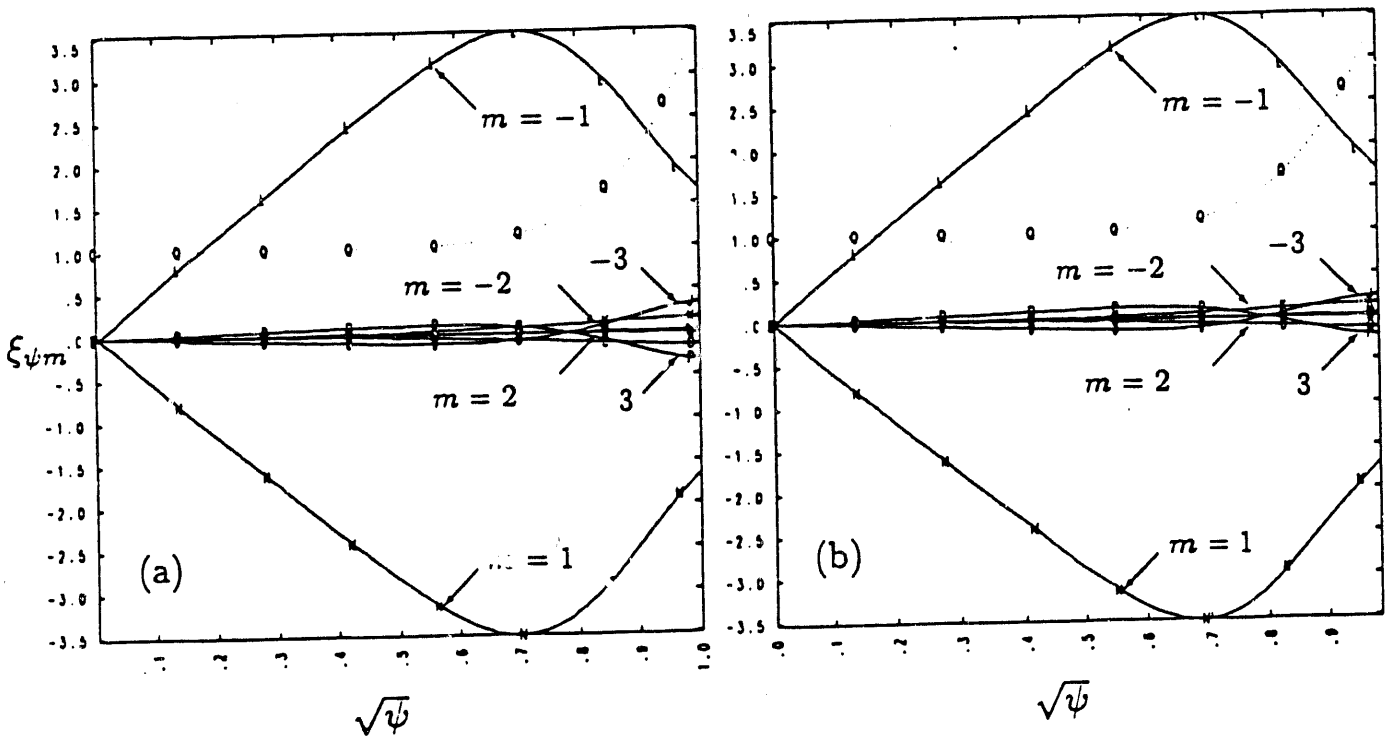

Figure 4

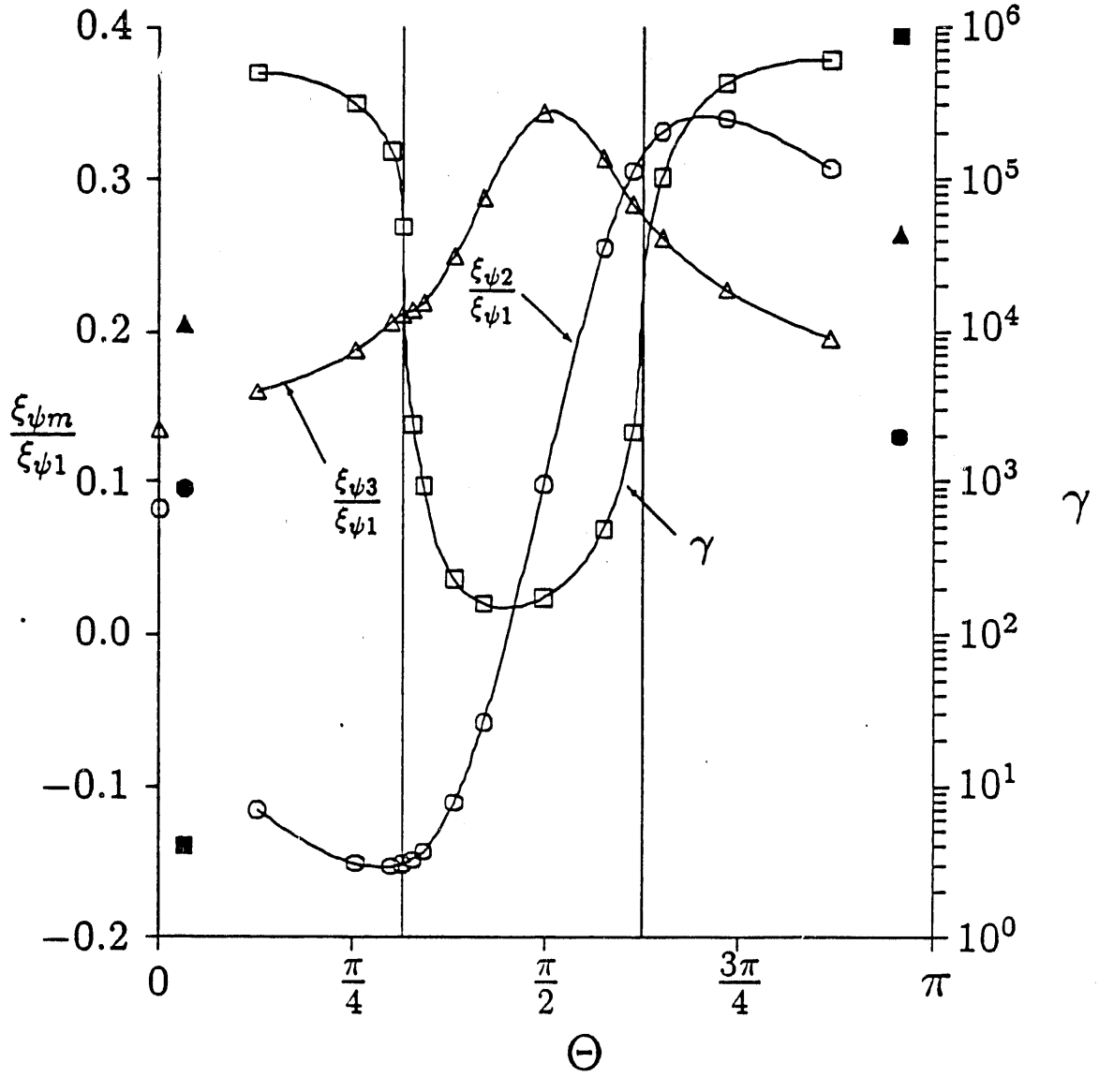
0.4
0.3
0.2
0.1
0.0
−0.1
−0.2
$\frac{\xi_{\psi m}}{\xi_{\psi 1}}$
10^6
10^5
10^4
10^3
10^2
10^1
10^0
γ
$\frac{\xi_{\psi 2}}{\xi_{\psi 1}}$
$\frac{\xi_{\psi 3}}{\xi_{\psi 1}}$
γ
0
$\frac{\pi}{4}$
$\frac{\pi}{2}$
$\frac{3\pi}{4}$
π
Θ

Figure 5

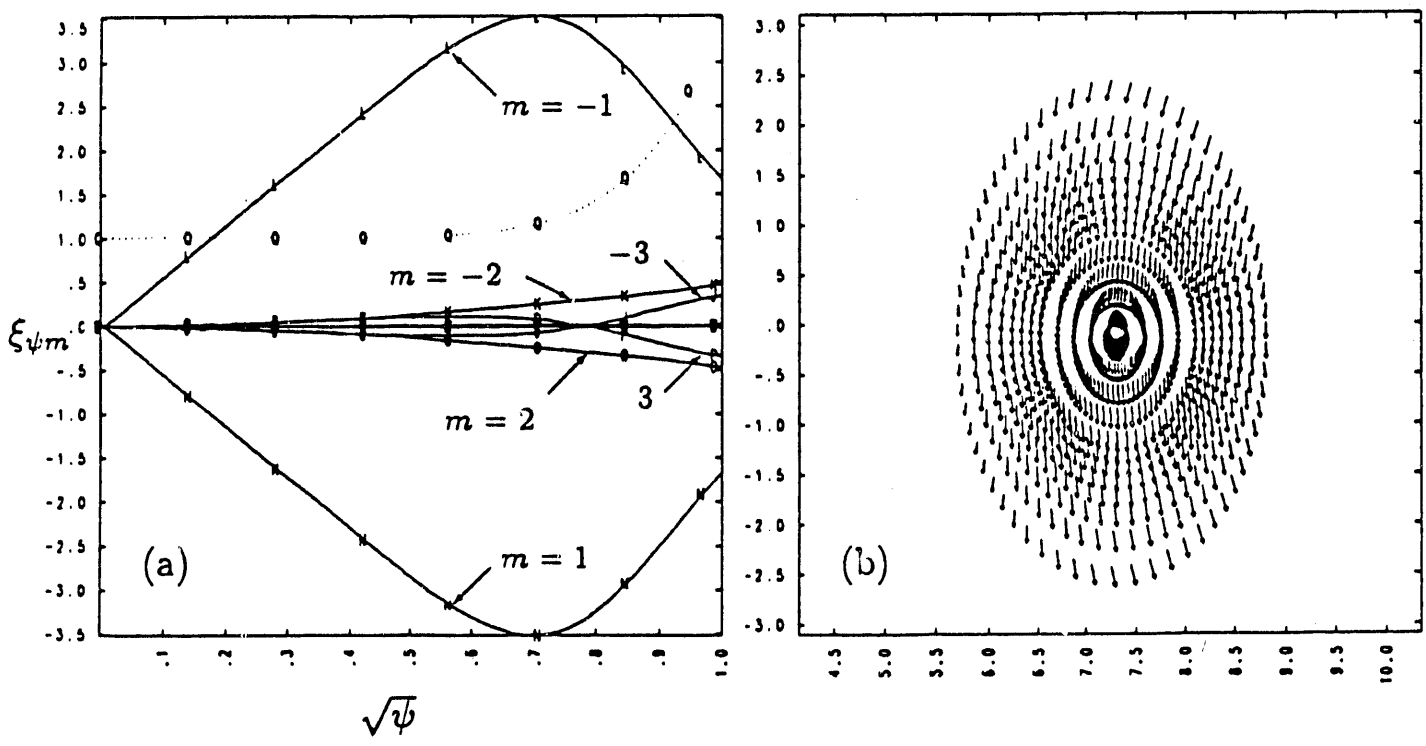

Figure 6

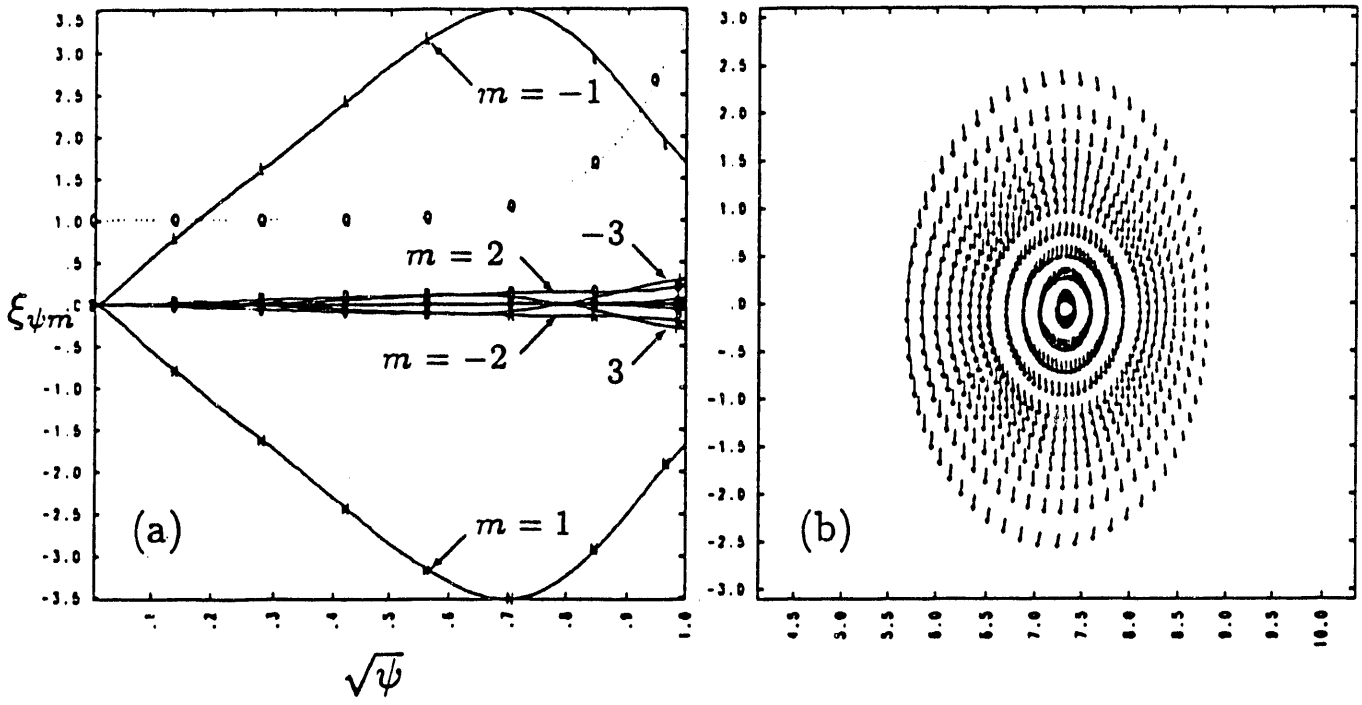

Figure 7

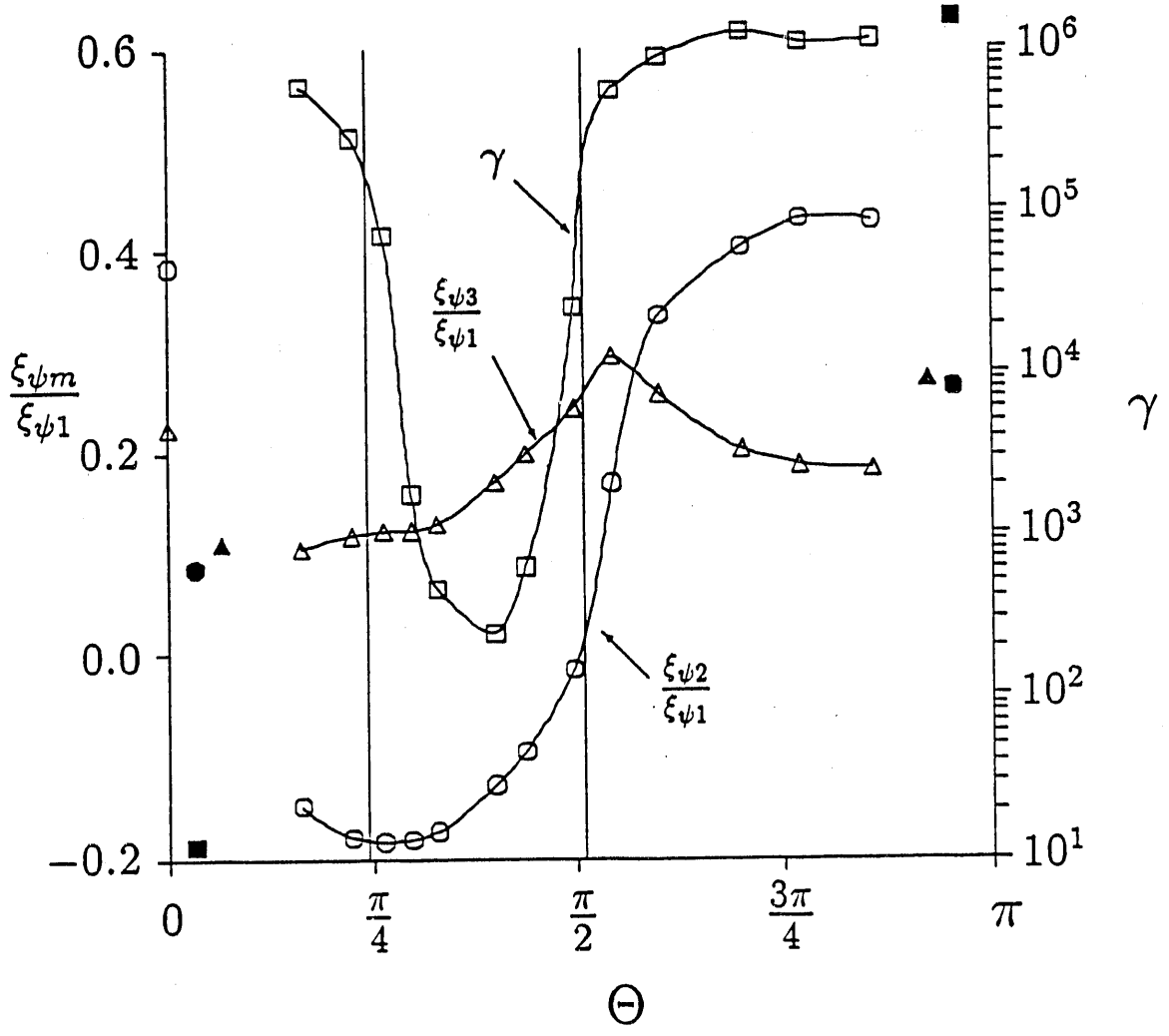
0.6
0.4
0.2
0.0
−0.2
$\frac{\xi_{\psi m}}{\xi_{\psi 1}}$
γ
$\frac{\xi_{\psi 3}}{\xi_{\psi 1}}$
$\frac{\xi_{\psi 2}}{\xi_{\psi 1}}$
10^6
10^5
10^4
10^3
10^2
10^1
γ
0
$\frac{\pi}{4}$
$\frac{\pi}{2}$
$\frac{3\pi}{4}$
π
Θ

Figure 8

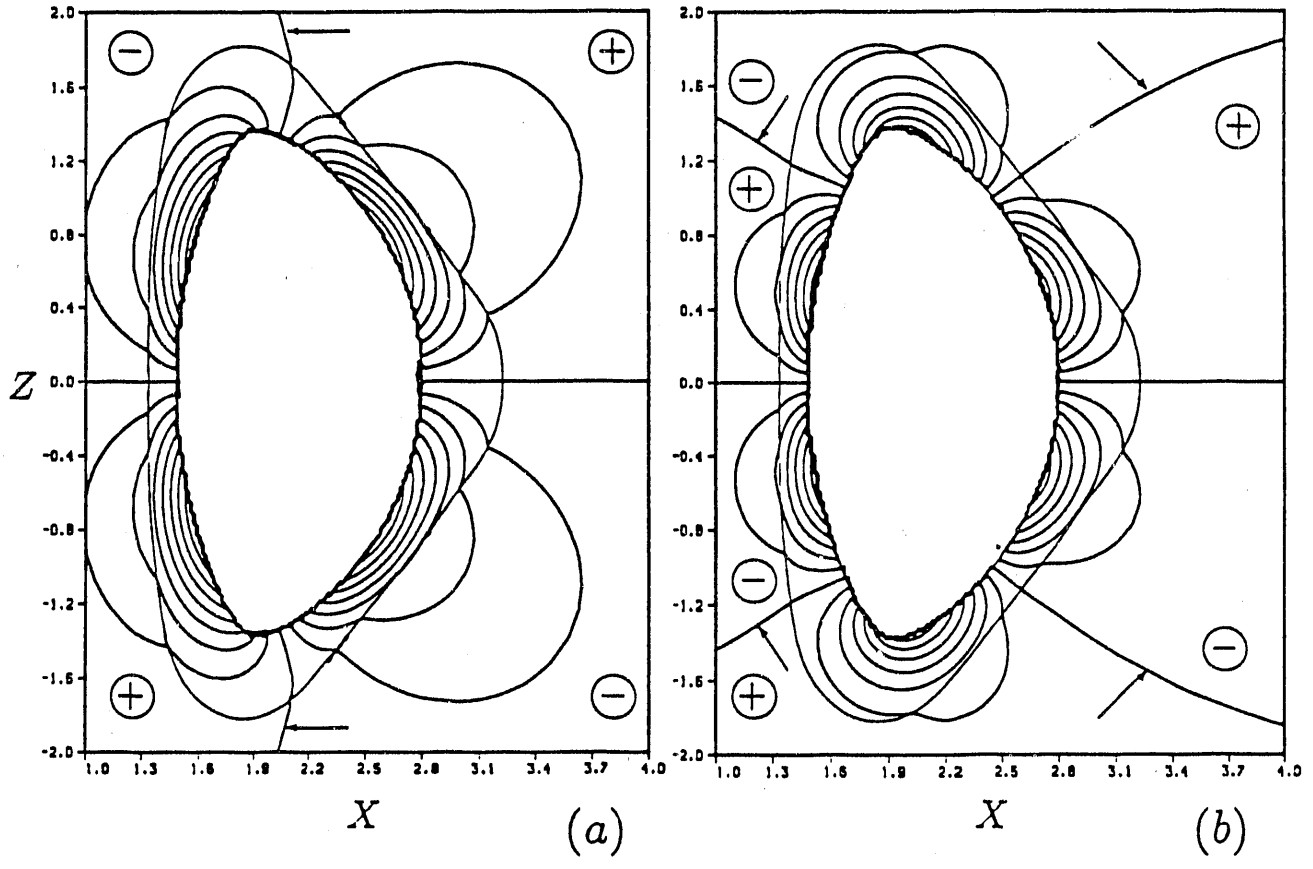

Figure 9

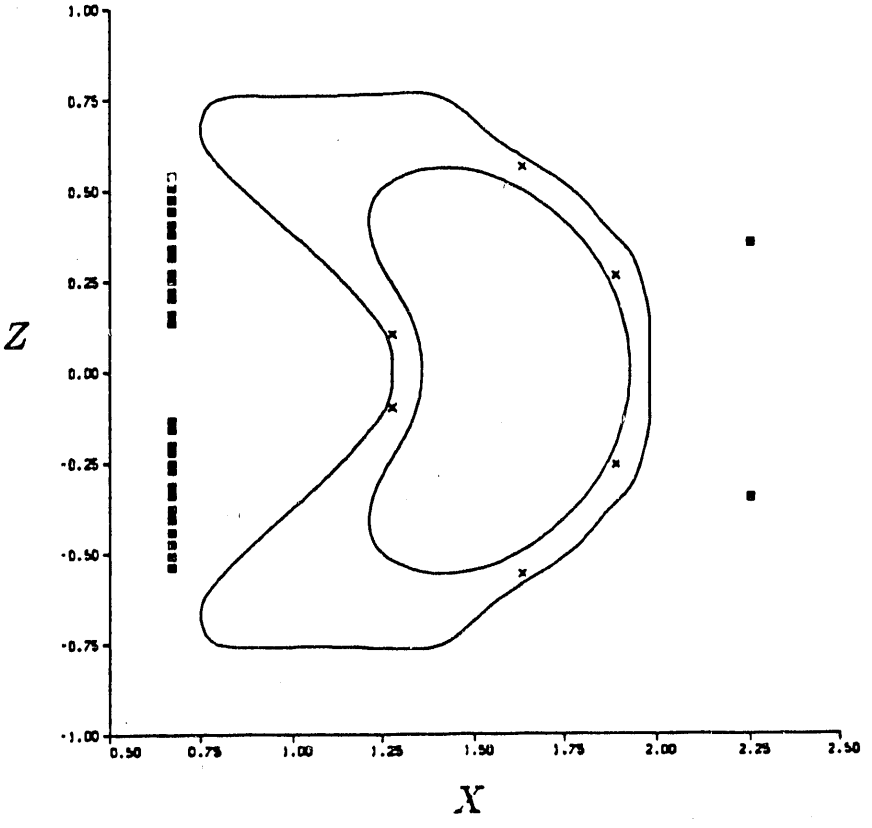
1.00
0.75
0.50
0.25
0.00
-0.25
-0.50
-0.75
-1.00
Z
0.50
0.75
1.00
1.25
1.50
1.75
2.00
2.25
2.50
X

Figure 10

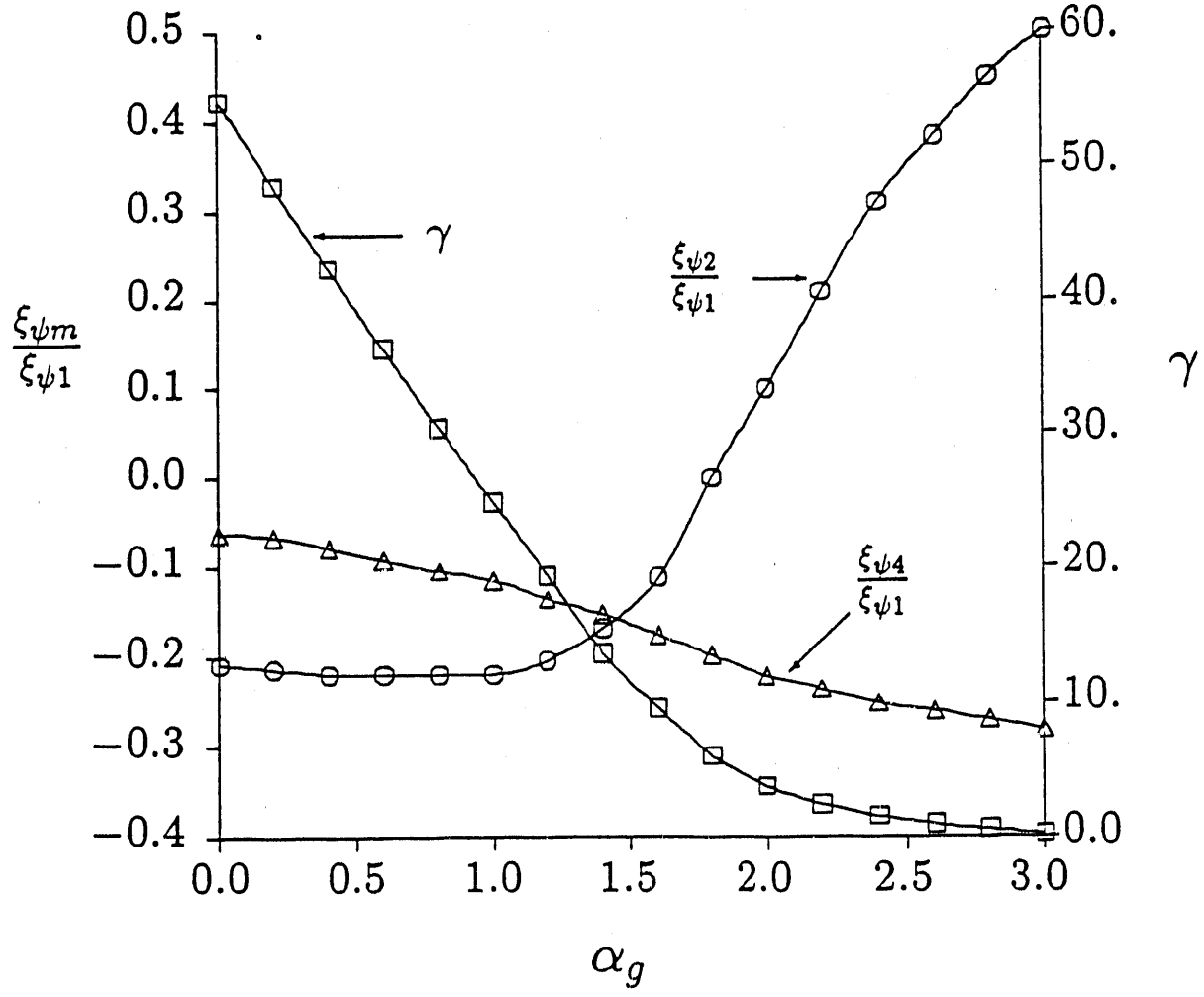
0.5
0.4
0.3
0.2
0.1
0.0
−0.1
−0.2
−0.3
−0.4
60.
50.
40.
30.
20.
10.
0.0
0.0
0.5
1.0
1.5
2.0
2.5
3.0
$\frac{\xi_{\psi m}}{\xi_{\psi 1}}$
γ
$\frac{\xi_{\psi 2}}{\xi_{\psi 1}}$
$\frac{\xi_{\psi 4}}{\xi_{\psi 1}}$
γ
α_g

Figure 11

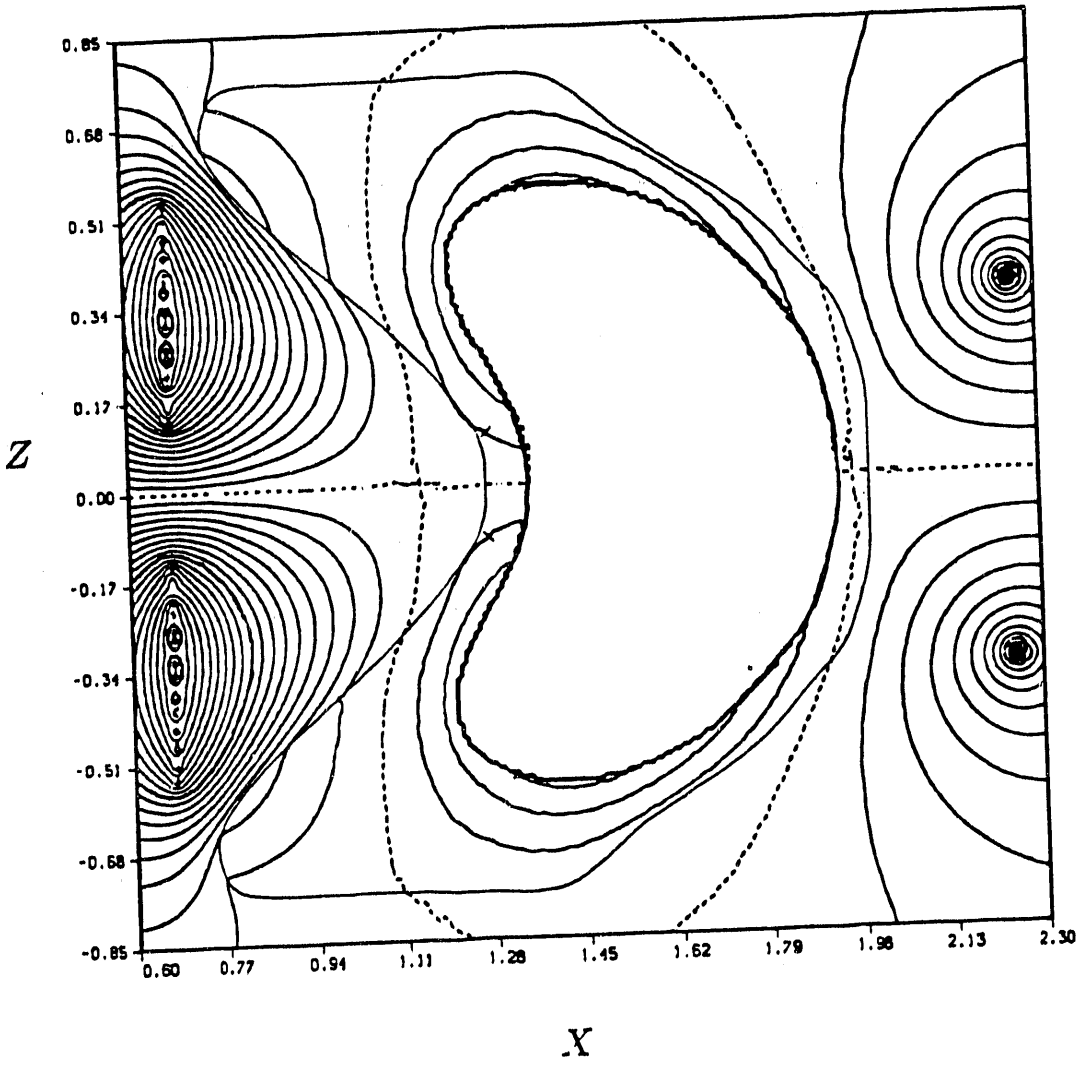
0.85
0.68
0.51
0.34
0.17
0.00
-0.17
-0.34
-0.51
-0.68
-0.85
Z
0.60
0.77
0.94
1.11
1.28
1.45
1.62
1.79
1.96
2.13
2.30
X

Figure 12

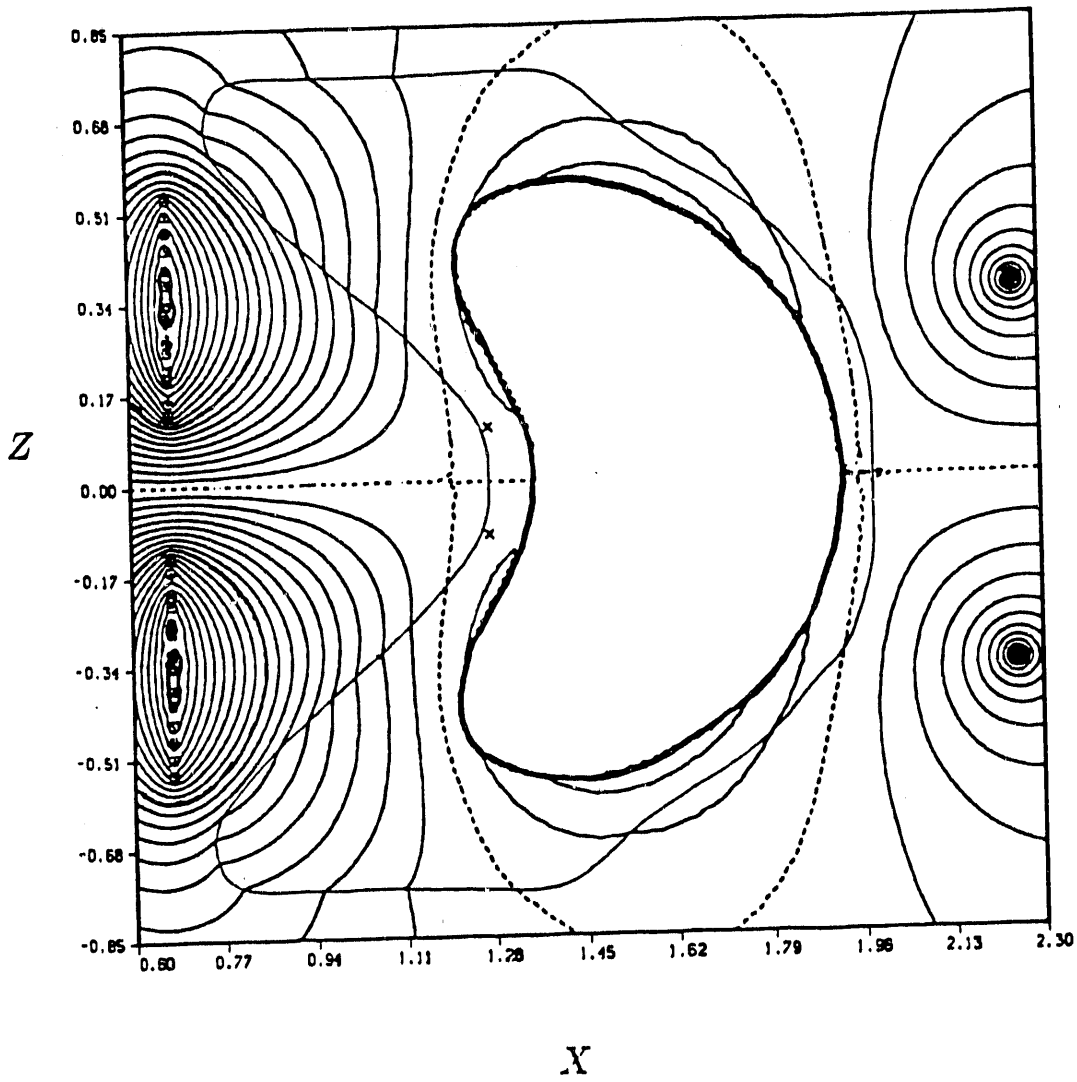
0.85
0.68
0.51
0.34
0.17
0.00
-0.17
-0.34
-0.51
-0.68
-0.85
0.60
0.77
0.94
1.11
1.28
1.45
1.62
1.79
1.96
2.13
2.30
Z
X

Figure 13

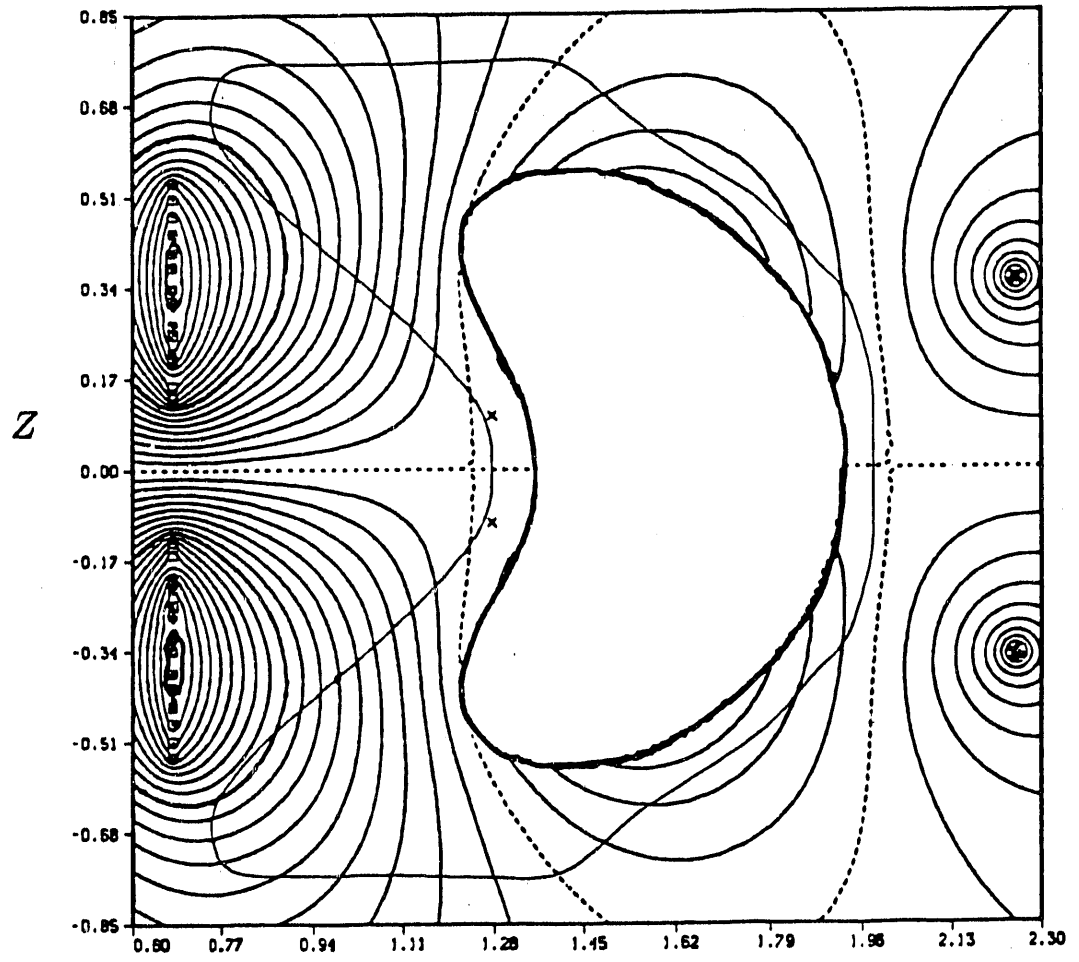
0.85
0.68
0.51
0.34
0.17
0.00
-0.17
-0.34
-0.51
-0.68
-0.85
Z
0.60
0.77
0.94
1.11
1.28
1.45
1.62
1.79
1.96
2.13
2.30
X

Figure 14

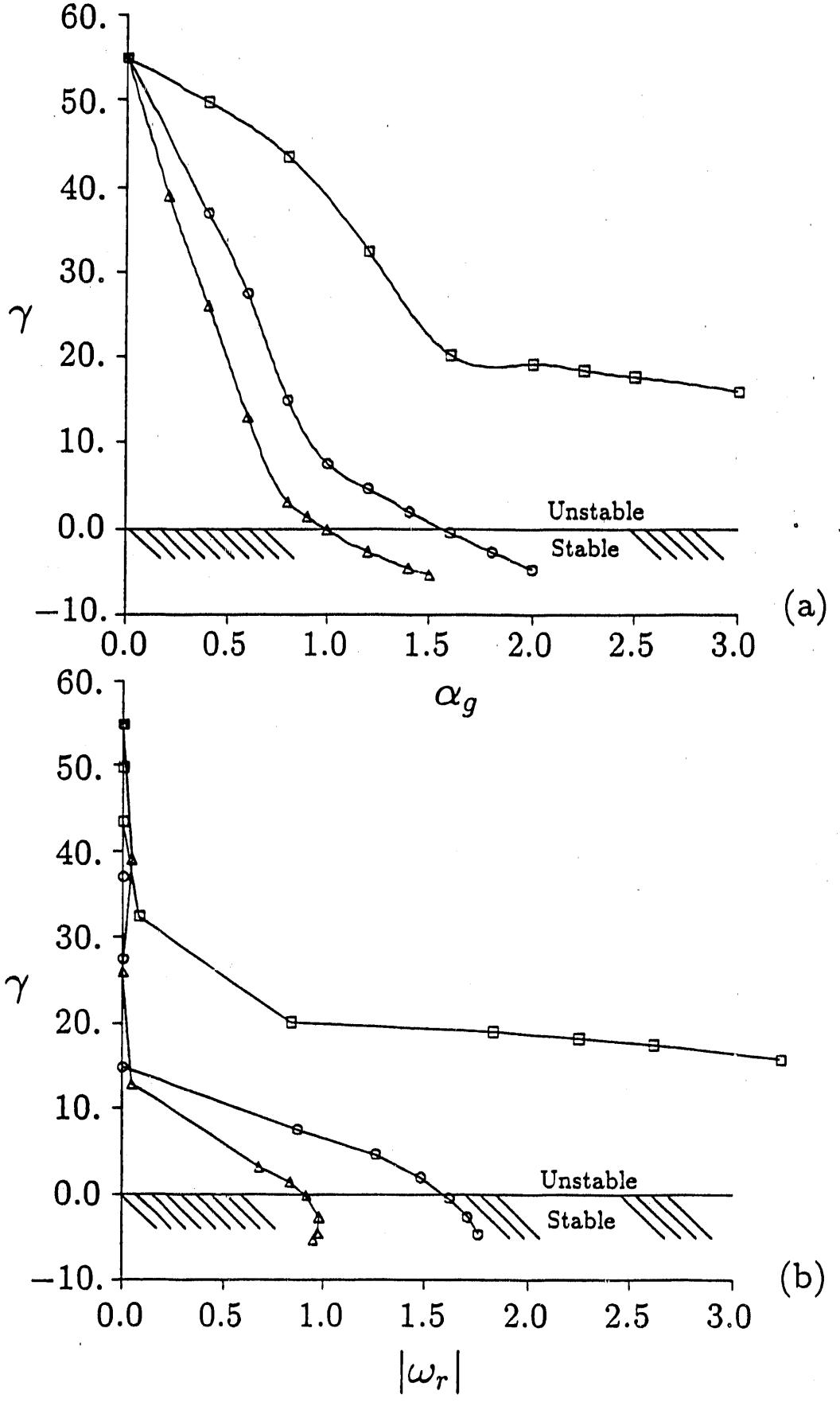
60.
50.
40.
30.
20.
10.
0.0
−10.
γ
Unstable
Stable
0.0
0.5
1.0
1.5
2.0
2.5
3.0
α_g
(a)
60.
50.
40.
30.
20.
10.
0.0
−10.
γ
Unstable
Stable
0.0
0.5
1.0
1.5
2.0
2.5
3.0
$|\omega_r|$
(b)

Figure 15

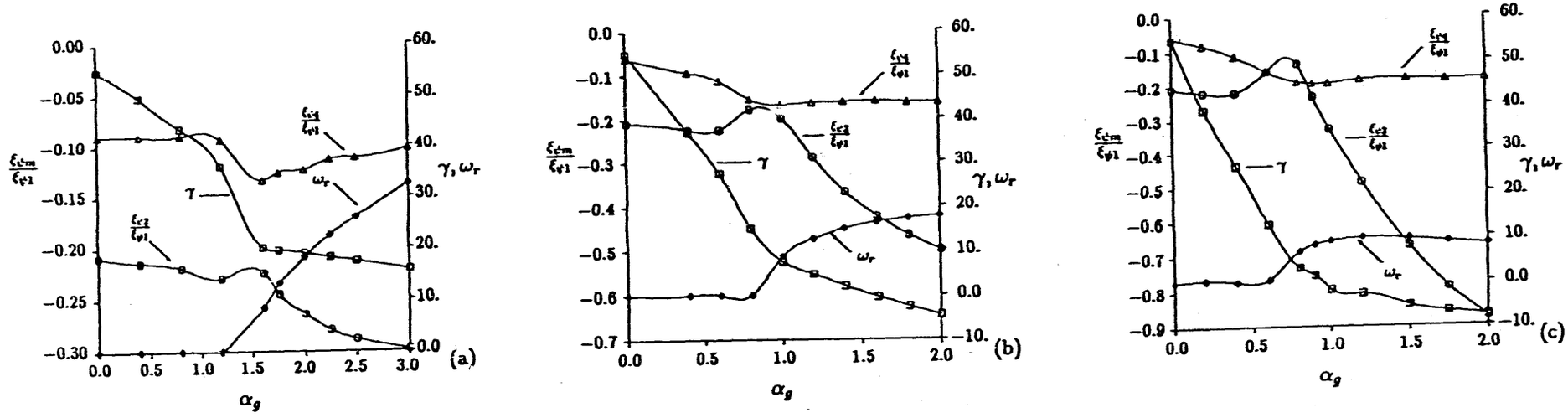

Figure 16

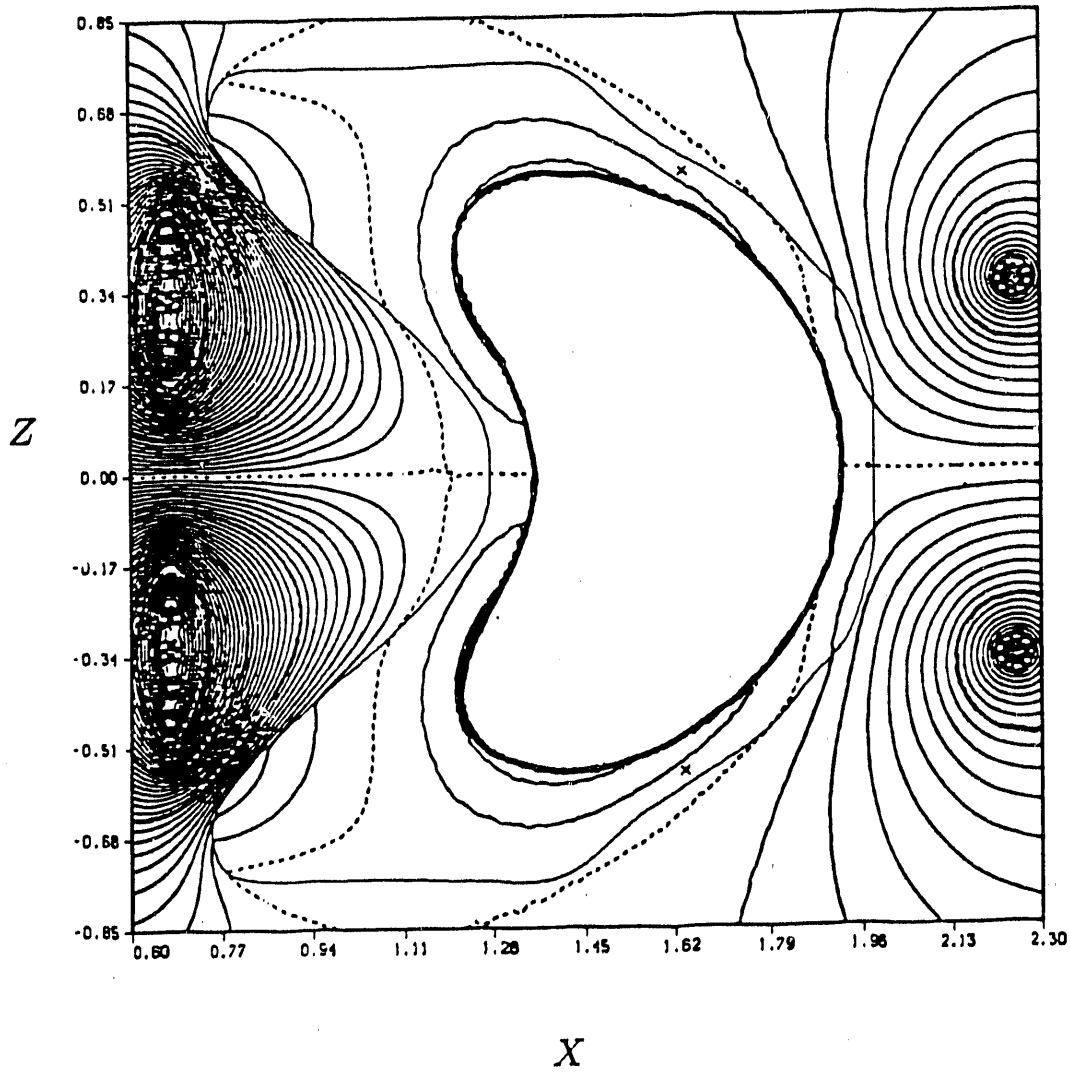
0.85
0.68
0.51
0.34
0.17
0.00
-0.17
-0.34
-0.51
-0.68
-0.85
0.60
0.77
0.94
1.11
1.28
1.45
1.62
1.79
1.96
2.13
2.30
Z
X

Figure 17

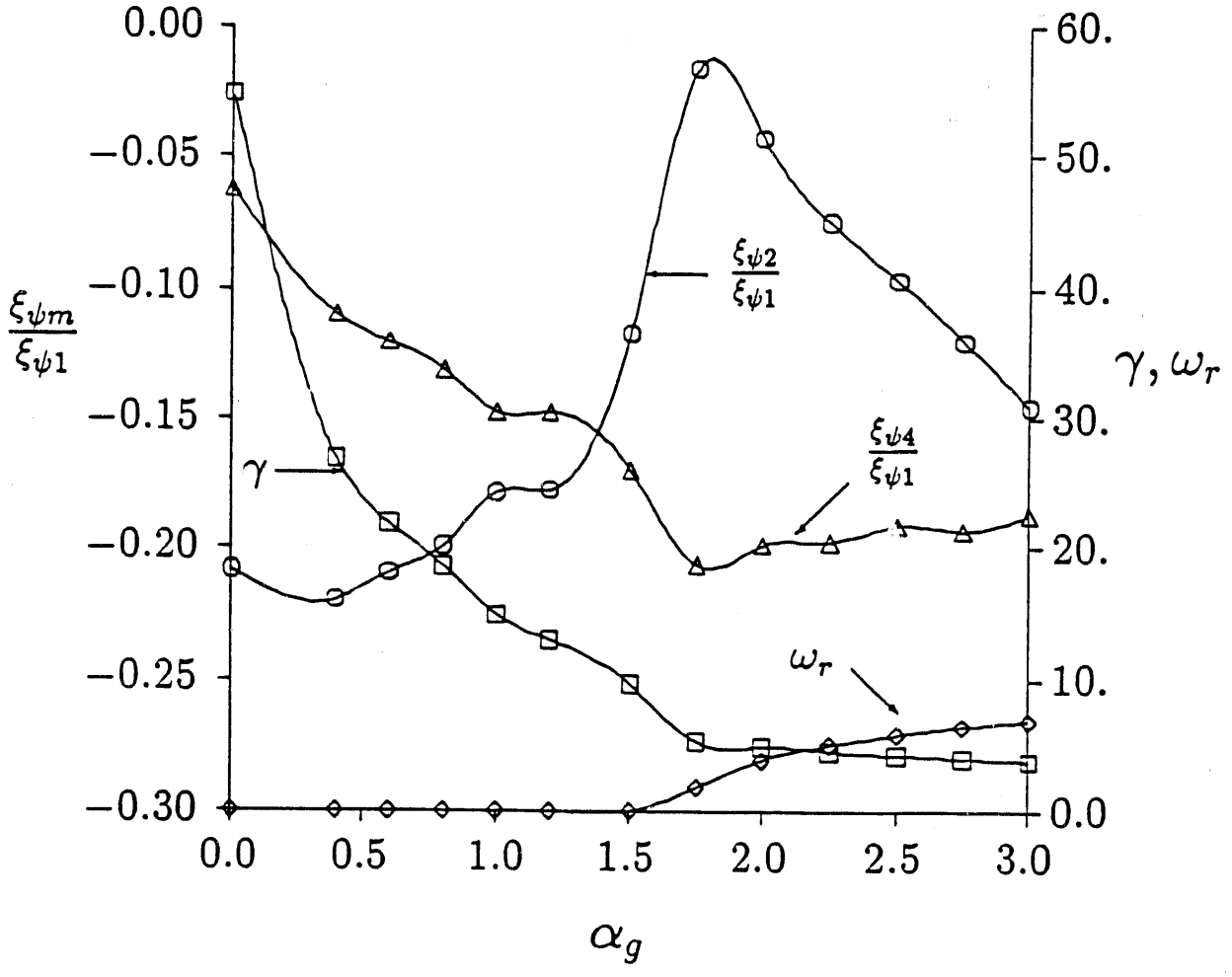
0.00
−0.05
−0.10
−0.15
−0.20
−0.25
−0.30
$\frac{\xi_{\psi m}}{\xi_{\psi 1}}$
60.
50.
40.
30.
20.
10.
0.0
γ, ω_r
0.0
0.5
1.0
1.5
2.0
2.5
3.0
α_g
$\frac{\xi_{\psi 2}}{\xi_{\psi 1}}$
$\frac{\xi_{\psi 4}}{\xi_{\psi 1}}$
γ
ω_r

Figure 18

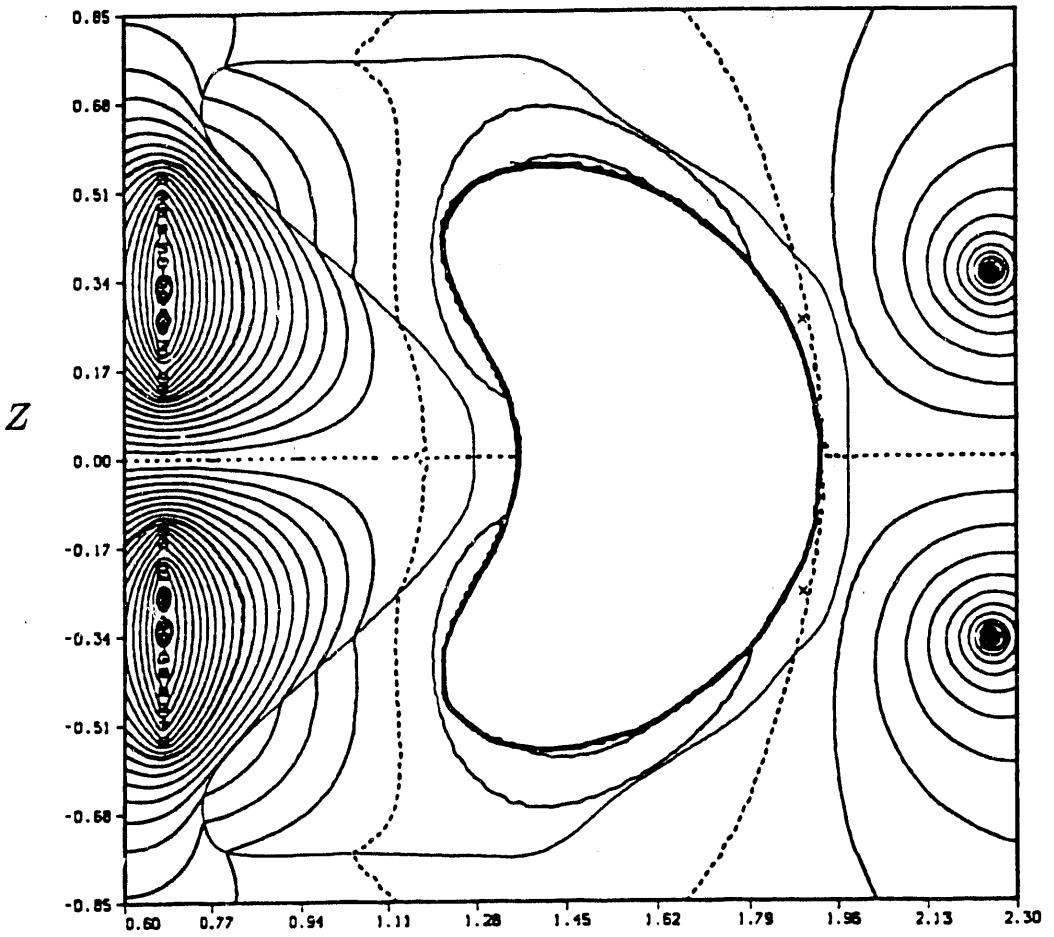
0.85
0.68
0.51
0.34
0.17
0.00
-0.17
-0.34
-0.51
-0.68
-0.85
Z
0.60
0.77
0.94
1.11
1.28
1.45
1.62
1.79
1.96
2.13
2.30
X

Figure 19

EXTERNAL DISTRIBUTION IN ADDITION TO UC-420

Dr. F. Paoloni, Univ. of Wollongong, AUSTRALIA
Prof. M.H. Brennan, Univ. of Sydney, AUSTRALIA
Plasma Research Lab., Australian Nat. Univ., AUSTRALIA
Prof. I.R. Jones, Flinders Univ, AUSTRALIA
Prof. F. Cap, Inst. for Theoretical Physics, AUSTRIA
Prof. M. Heindler, Institut für Theoretische Physik, AUSTRIA
Prof. M. Goossens, Astronomisch Instituut, BELGIUM
Ecole Royale Militaire, Lab. de Phy. Plasmas, BELGIUM
Commission-European, DG. XII-Fusion Prog., BELGIUM
Prof. R. Boucique, Rijksuniversiteit Gent, BELGIUM
Dr. P.H. Sakanaka, Instituto Fisica, BRAZIL
Instituto Nacional De Pesquisas Espaciais-INPE, BRAZIL
Documents Office, Atomic Energy of Canada Ltd., CANADA
Dr. M.P. Bachynski, MPB Technologies, Inc., CANADA
Dr. H.M. Skarsgard, Univ. of Saskatchewan, CANADA
Prof. J. Teichmann, Univ. of Montreal, CANADA
Prof. S.R. Sreenivasan, Univ. of Calgary, CANADA
Prof. T.W. Johnston, INRS-Energie, CANADA
Dr. R. Bolton, Centre canadien de fusion magnétique, CANADA
Dr. C.R. James,, Univ. of Alberta, CANADA
Dr. P. Lukác, Komenského Universzita, CZECHO-SLOVAKIA
The Librarian, Culham Laboratory, ENGLAND
Library, R61, Rutherford Appleton Laboratory, ENGLAND
Mrs. S.A. Hutchinson, JET Library, ENGLAND
Dr. S.C. Sharma, Univ. of South Pacific, FIJI ISLANDS
P. Mähönen, Univ. of Helsinki, FINLAND
Prof. M.N. Bussac, Ecole Polytechnique,, FRANCE
C. Mouttet, Lab. de Physique des Milieux Ionisés, FRANCE
J. Radet, CEN/CADARACHE - Bat 506, FRANCE
Prof. E. Economou, Univ. of Crete, GREECE
Ms. C. Rinni, Univ. of Ioannina, GREECE
Dr. T. Mual, Academy Bibliographic Ser., HONG KONG
Preprint Library, Hungarian Academy of Sci., HUNGARY
Dr. B. DasGupta, Saha Inst. of Nuclear Physics, INDIA
Dr. P. Kaw, Inst. for Plasma Research, INDIA
Dr. P. Rosenau, Israel Inst. of Technology, ISRAEL
Librarian, International Center for Theo Physics, ITALY
Miss C. De Palo, Associazione EURATOM-ENEA , ITALY
Dr. G. Grosso, Istituto di Fisica del Plasma, ITALY
Prof. G. Rostangni, Istituto Gas Ionizzati Del Cnr, ITALY
Dr. H. Yamato, Toshiba Res & Devel Center, JAPAN
Prof. I. Kawakami, Hiroshima Univ., JAPAN
Prof. K. Nishikawa, Hiroshima Univ., JAPAN
Director, Japan Atomic Energy Research Inst., JAPAN
Prof. S. Itoh, Kyushu Univ., JAPAN
Research Info. Ctr., National Instit. for Fusion Science, JAPAN
Prof. S. Tanaka, Kyoto Univ., JAPAN
Library, Kyoto Univ., JAPAN
Prof. N. Inoue, Univ. of Tokyo, JAPAN
Secretary, Plasma Section, Electrotechnical Lab., JAPAN
S. Mori, Technical Advisor, JAERI, JAPAN
Dr. O. Mitarai, Kumamoto Inst. of Technology, JAPAN
J. Hyeon-Sook, Korea Atomic Energy Research Inst., KOREA
D.I. Choi, The Korea Adv. Inst. of Sci. & Tech., KOREA
Prof. B.S. Liley, Univ. of Waikato, NEW ZEALAND
Inst of Physics, Chinese Acad Sci PEOPLE'S REP. OF CHINA
Library, Inst. of Plasma Physics, PEOPLE'S REP. OF CHINA
Tsinghua Univ. Library, PEOPLE'S REPUBLIC OF CHINA
Z. Li, S.W. Inst Physics, PEOPLE'S REPUBLIC OF CHINA
Prof. J.A.C. Cabral, Instituto Superior Tecnico, PORTUGAL
Dr. O. Petrus, AL I CUZA Univ., ROMANIA
Dr. J. de Villiers, Fusion Studies, AEC, S. AFRICA
Prof. M.A. Hellberg, Univ. of Natal, S. AFRICA
Prof. D.E. Kim, Pohang Inst. of Sci. & Tech., SO. KOREA
Prof. C.I.E.M.A.T, Fusion Division Library, SPAIN
Dr. L. Stenflo, Univ. of UMEA, SWEDEN
Library, Royal Inst. of Technology, SWEDEN
Prof. H. Wilhelmson, Chalmers Univ. of Tech., SWEDEN
Centre Phys. Des Plasmas, Ecole Polytech, SWITZERLAND
Bibliotheek, Inst. Voor Plasma-Fysica, THE NETHERLANDS
Asst. Prof. Dr. S. Cakir, Middle East Tech. Univ., TURKEY
Dr. V.A. Glukhikh,Sci. Res. Inst. Electrophys.I Apparatus, USSR
Dr. D.D. Ryutov, Siberian Branch of Academy of Sci., USSR
Dr. G.A. Eliseev, I.V. Kurchatov Inst., USSR
Librarian, The Ukr.SSR Academy of Sciences, USSR
Dr. L.M. Kovrizhnykh, Inst. of General Physics, USSR
Kernforschungsanlage GmbH, Zentralbibliothek, W. GERMANY
Bibliothek, Inst. Für Plasmaforschung, W. GERMANY
Prof. K. Schindler, Ruhr-Universität Bochum, W. GERMANY
Dr. F. Wagner, (ASDEX), Max-Planck-Institut, W. GERMANY
Librarian, Max-Planck-Institut, W. GERMANY
Prof. R.K. Janev, Inst. of Physics, YUGOSLAVIA

END

DATE FILMED

2/24/92